REVIEW

Electrode materials and reaction mechanisms in solid oxide fuel cells: a brief review

I. Performance-determining factors

Ekaterina V. Tsipis · Vladislav V. Kharton

Abstract This work is focused on the comparative analysis of electrochemical and transport properties in the major families of cathode and anode compositions for intermediate-temperature solid oxide fuel cells (SOFCs) and materials science-related factors affecting electrode performance. The first part presents a brief overview of the electrochemical and chemical reactions in SOFCs, specific rate-determining steps of the electrode processes, solid oxide electrolyte ceramics, and effects of partial oxygen ionic and electronic conductivities in the SOFC components. The aspects associated with materials compatibility, thermal expansion, stability, and electrocatalytic behavior are also briefly discussed. Primary attention is centered on the experimental data and approaches reported during the last 10–15 years, reflecting the main challenges in the field of materials development for the ceramic fuel cells.

Keywords Intermediate-temperature SOFCs ·
Solid oxide electrolyte · Mixed conductor ·
Electrode compositions · Oxygen ionic transport

Introduction

Solid oxide fuel cell (SOFC) is a type of fuel cells where the chemical energy of a gaseous fuel is converted into electrical energy due to electrochemical reactions at two electrodes separated by an oxygen ion-conducting ceramic membrane. SOFCs operate at elevated temperatures,

770–1270 K, when the interfacial processes and ionic transport in the solid electrolyte are fast enough. With respect to other types of fuel cells, such as alkaline fuel cell (AFC), polymer electrolyte membrane fuel cell (PEMFC), phosphoric acid fuel cell (PAFC), and molten carbonate fuel cell (MCFC), SOFCs attract great interest due to their high-energy conversion efficiency, fuel flexibility including the prospects to directly operate on natural gas and biogas, environmental safety, and a possibility to recover exhaust heat [1–12]. Practical application of SOFCs is, however, still limited for economical reasons, particularly as a result of the high costs of materials and processing technologies.

A single SOFC comprises, at least, one dense solid-electrolyte membrane in contact with porous anode and cathode onto which a fuel and an oxidant are continuously supplied; the power is generated due to the reduction of the oxidant (usually atmospheric oxygen) at the cathode and fuel oxidation by the O^{2-} anions diffused through the electrolyte at the anode. A variety of other catalytic processes affecting SOFC performance, such as the water gas shift reaction and reforming of hydrocarbons, may also occur over the anode layers [1, 2, 4, 6, 7, 9]. The SOFC operation principles determine key requirements to the component materials. First of all, the solid electrolyte (SE) should possess maximum ionic conductivity and minimum electronic transport over a wide range of the oxygen chemical potentials. The anode and cathode should provide a fast electronic conduction and high catalytic activity towards fuel oxidation and oxygen reduction, respectively, and should also have an appropriate microstructure to avoid mass transport limitations. Furthermore, all the components should be chemically and thermomechanically compatible, stable under the operation and fabrication conditions, and should exhibit minimum chemical expansion and cation interdiffusion. These stringent requirements have resulted

E. V. Tsipis · V. V. Kharton (✉)
Department of Ceramics and Glass Engineering, CICECO,
University of Aveiro,
3810-193 Aveiro, Portugal
e-mail: kharton@ua.pt

in the continuous search for optimum SOFC materials, which started in the 1930s. The fuel cell operating at 1270 K with MgO–ZrO$_2$ or Y$_2$O$_3$–ZrO$_2$ electrolytes, Fe$_3$O$_4$ cathodes, and iron or carbon anodes was reported in 1937 [13]. In the 1960s–1970s, Pt electrodes were widely used due to their stability, high conductivity, and a substantial catalytic activity (e.g., [2, 14–16]). Later, platinum was substituted with less expensive components, primarily Ni-based cermets for the anodes and various perovskite compounds for the cathodes [2–4, 6, 10, 12, 15–18]. These materials, in particular (La,Sr)MnO$_{3-\delta}$ (LSM) perovskite cathodes and the yttria-stabilized zirconia (YSZ) solid electrolytes, are commonly used in SOFCs and other high-temperature electrochemical devices up to now [1–10, 19]. Table 1 and Fig. 1 present selected examples of the maximum power density in planar SOFCs, listing several state-of-the-art materials.

One of the most important challenges in SOFC developments relates to lowering the operation temperatures down to 770–1070 K, simultaneously preserving a high power density and durability. The intermediate-temperature (IT) SOFCs provide serious technological and economical advantages, including: (1) reduced manufacturing costs, particularly owing to the relatively inexpensive construction materials, such as stainless steels for interconnects; (2) improved mechanical durability of the stack due to suppressed materials degradation caused by the high operating temperatures and by thermal cycling, and also a possibility to avoid the use of fragile glass–ceramic sealants for hermetization; (3) enhanced efficiency of the kW-scale generators used without integration with gas turbines [3, 4, 6, 33]. Decreasing the operating temperature increases the role of electrode polarization as performance-limiting factor because the apparent activation energies for the interfacial processes are, as a rule, higher than those for ionic transport
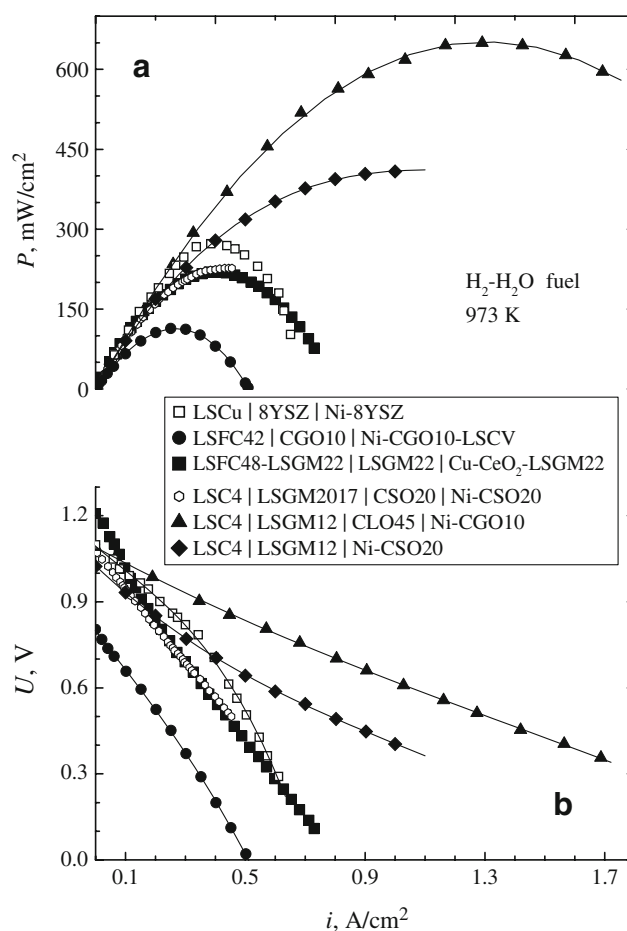

Fig. 1 Current dependencies of the specific power density (a) and voltage (b) for various planar SOFCs [27–32]. *LSCu*, *LSC4*, *LSFC42* and *LSFC48*, *LSGM12*, *LSGM22* and *LSGM2017*, *CGO10*, *CSO20*, *CLO45*, and *LSCV* denote La$_{0.75}$Sr$_{0.25}$CuO$_{2.5-\delta}$, La$_{0.6}$Sr$_{0.4}$CoO$_{3-\delta}$, La$_{1-x}$S$_x$Fe$_{1-y}$Co$_y$O$_{3-\delta}$ (x=0.4 and y=0.2, and x=0.4 and y=0.8), La$_{1-x}$S$_x$Ga$_{1-y}$Mg$_y$O$_{3-\delta}$ (x=0.1 and y=0.2, x=0.2 and y=0.2, and x=0.20 and y=0.17), Ce$_{0.90}$Gd$_{0.10}$O$_{2-\delta}$, Ce$_{0.80}$Sm$_{0.20}$O$_{2-\delta}$, Ce$_{0.55}$La$_{0.45}$O$_{2-\delta}$, and La$_{0.8}$Sr$_{0.2}$Cr$_{0.98}$V$_{0.02}$O$_{3-\delta}$, respectively

Table 1 Comparison of the maximum power densities (*P*) demonstrated by planar single SOFCs using hydrogen as fuel

Cell type	Electrolyte	Cathode	Anode	T (K)	P (W/cm^2)	Ref.
Anode-supported	YSZ	YSZ-La$_{0.85}$Sr$_{0.15}$MnO$_3$	Ni-YSZ	1073	0.7	[20]
Anode-supported	YSZ	YSZ-La$_{0.8}$Sr$_{0.2}$MnO$_3$	Ni-YSZ	923–1073	0.8–1.8	[21]
Anode-supported	YSZ	YSZ-La$_{0.8}$Sr$_{0.2}$MnO$_3$	Cu-CeO$_2$	1073	0.31	[5]
Anode-supported	Ce$_{0.8}$Gd$_{0.2}$O$_2$ (CGO20)	La$_{0.8}$Sr$_{0.2}$Fe$_{0.8}$Co$_{0.2}$O$_3$ (LSFC22)	Ni-CGO	773	0.14	[22]
Anode-supported	Double-layer yttria-doped ceria and zirconia (CYO^a-YSZ)	La$_{0.8}$Sr$_{0.2}$Fe$_{0.8}$Co$_{0.2}$O$_3$ -CYO composite	Ni-YSZ	973–1073	0.47–0.89	[23]
Cathode-supported	YSZ with cathode and anode CYO interlayers	La$_{0.85}$Sr$_{0.15}$MnO$_3$	Ni-YSZ	973–1073	0.30–0.87	[24]
Electrolyte-supported	La$_{0.9}$Sr$_{0.1}$Ga$_{0.8}$Mg$_{0.2}$O$_3$ (LSGM12)	Sm$_{0.6}$Sr$_{0.4}$CoO$_3$	Ni	1073	0.44	[25]
Electrolyte-supported	La$_{0.9}$Sr$_{0.1}$Ga$_{0.8}$Mg$_{0.2}$O$_3$+2 wt% Al$_2$O$_3$ with cathode and anode Ce$_{0.8}$Sm$_{0.2}$O$_2$ (CSO20) interlayers	Pr$_{0.6}$Sr$_{0.4}$MnO$_3$-CSO20 composite	Ni-YSZ	1073	0.245	[26]

^{a} Exact composition of CYO was not specified.

in solid oxide electrolytes [34, 35]. This makes it necessary to develop novel cathode and anode compositions with superior electrochemical activity in the intermediate-temperature range, and to optimize the cell fabrication technologies and electrode microstructures [3, 4, 33–38]. To reduce ohmic losses, decreasing of the SE membrane thickness and/or elaboration of alternative high-conductivity electrolytes is also inevitable. Despite the significant progress achieved during the last 10–15 years, the problems related to high costs and availability of existing technological solutions, insufficient stability of the IT SOFC components and interfaces and scarce information on the electrochemical reactions mechanisms are still of primary importance.

The aim of this review is to compare the electrochemical activity, transport properties, and thermal expansion of the IT SOFC electrode materials, and to analyze the major factors governing electrode performance. In this brief review, it was impossible to cover all promising compositions, important theoretical aspects, and numerous technological approaches developed in the field of SOFCs. Priority has been given mainly to the well-established materials and approaches, the applicability of which was validated, at least, by several research groups; selection of the references for this review is focused on the last 10–15 years. The first part is centered on the basic mechanisms of cathodic and anodic reactions, simplified analytical models for their description, and the materials science-related factors relevant to electrode polarization. As the electrochemical processes are usually affected by electrolyte properties, a brief survey of literature data on the ionic and electronic conductivities and thermal expansion of the SE ceramics is also presented. Readers interested further in the microscopic and macro-scale models for the interfacial processes, electrode processing, ion diffusion mechanisms, and specific properties of solid-electrolyte and mixed-conducting materials listed in this work are referred to comprehensive reviews and monographs [39–52].

Solid oxide electrolytes: an overview

Due to growing interest in environmentally benign and energy-saving technologies, developments in the field of oxygen ion-conducting electrolytes were considerably intensified during the last two decades. A series of novel ionic conductors have been reported, including $LaGaO_3$-based perovskites [25, 53, 54], derivatives of $Bi_4V_2O_{11}$ (BIMEVOX) [55] and $La_2Mo_2O_9$ (LAMOX) [56], several pyrochlores with relatively high ionic transport such as $(Gd, Ca)_2Ti_2O_{7-\delta}$ [57], and apatite materials derived from $Ln_{10-x}Si_6O_{26\pm\delta}$ where Ln is a rare-earth cation [58–61]. In many aspects, such materials exhibit an improved performance

with respect to ZrO_2-, ThO_2-, HfO_2-, CeO_2- and δ-Bi_2O_3-based solid electrolytes known and used since the early 1960s–1970s [3, 4, 6, 14–20, 33, 39–41, 46–49, 62, 63]. On the other hand, the rapid developments in this field have resulted in a significant lack of knowledge regarding key properties of these potential new electrolytes; some of these materials are strictly speaking mixed ionic–electronic conductors (MIECs) rather than perfect solid electrolytes and, in many cases, are unstable under the SOFC operating conditions. In this review, such families of ionic conductors are excluded from consideration. For instance, BIMEVOX and δ-Bi_2O_3-based phases possess high ionic conductivity with respect to other solid electrolytes, but suffer from very high thermal expansion coefficients (TECs), substantial electronic transport, thermodynamic instability under reducing conditions, volatilization of bismuth oxide, and extremely high chemical reactivity [47, 63]. Hence, the applicability of these oxides in SOFCs is almost impossible. The LAMOX family also displays, in general, excessively high TECs and easy reducibility, leading to an appearance of significant n-type electronic conductivity in moderately reducing atmospheres and even in air at temperatures above 1000–1050 K [47, 64]. The derivatives of brownmillerite-like $Ba_2In_2O_5$ exhibit a fast degradation under the SOFC operation conditions, particularly due to the interaction with water vapor and CO_2 [65]. As for these newly reported materials, the applicability of well-established ionic conductors based on doped HfO_2, ThO_2, and $LnAlO_3$ is also hampered by their specific disadvantages, including the low ionic conductivity and relatively high electronic transport compared to the ZrO_2- and CeO_2-based analogues, and radioactivity of thoria [39, 62]. Consequently, possible choice of the IT SOFC electrolytes is still limited, mainly to $LaGaO_3$-, CeO_2-, ZrO_2- and $La_{10-x}Si_6O_{26\pm\delta}$-based systems.

Ionic conductivity

The maximum ionic conduction in zirconia-based phases is observed when the concentration of acceptor rare-earth or alkaline-earth dopant cations is close to the minimum necessary to completely stabilize the cubic fluorite-type polymorph; further additions decrease the ionic transport due to the increasing association of the oxygen vacancies and dopant cations into complex defects of low mobility [16, 39, 41, 46–48, 66–68]. The latter tendency rises with increasing difference between the host and dopant cation radii. Because the size of Zr^{4+} is smaller than that of the trivalent rare-earth cations, the maximum ionic conductivity in binary ZrO_2–Ln_2O_3 systems is observed in the cubic solid solutions where Ln=Sc, Yb, Lu, or Y. Taking into account the costs of rare-earth components, YSZ is used for most practical applications up to now. Although scandia-

stabilized zirconia (SSZ) has a significantly higher conductivity (Fig. 2), this group of electrolytes is characterized with fast ageing caused by partial ordering and decomposition of metastable cubic and rhombohedral solid solutions in the intermediate-temperature range [41, 47, 66–68]. The highest conductivity levels in $Zr_{1-x}Y_xO_{2-x/2}$ and $Zr_{1-x}Sc_xO_{2-x/2}$ ceramics are observed at $x=0.08-0.11$ and $0.09-0.11$, respectively. In practice, however, the electrolyte compositions with higher dopant content are often used due to lower degradation rate at intermediate temperatures. Among the conventional compositions, one should mention 8 mol% Y_2O_3-stabilized zirconia ($Zr_{0.85}Y_{0.15}O_{1.93}$ or 8YSZ). Doping of ZrO_2 with alkaline-earth metal cations (A^{2+}) is much less effective compared to rare-earth dopants; this results from a higher tendency to defect association and from a lower thermodynamic stability of the fluorite-like phases in ZrO_2–AO systems [16, 39]. At temperatures below 1470 K, the cubic $Zr(A)O_{2-\delta}$ solid solutions are stable only for A=Ca. The conductivity of $Zr_{1-x}Ca_xO_{2-x}$

with maximum at $x=0.13-0.15$ is substantially lower than that of $Zr_{1-x}Ln_xO_{2-x/2}$.

If compared to stabilized zirconia, the cubic fluorite-type phases based on $CeO_{2-\delta}$ possess a considerably faster ionic transport predominant under oxidizing conditions. In addition, doped ceria exhibits no phase transitions at atmospheric $p(O_2)$ in the whole temperature range important for the fabrication and operation of SOFCs. Among ceria-based solid solutions, the highest ionic conductivity is found for $Ce_{1-x}Ln_xO_{2-\delta}$ where Ln=Gd or Sm, $x=0.10-0.20$ [6, 62, 71, 72, 77]. The solubility of alkaline-earth cations in the ceria lattice is quite limited and decreases on cooling, leading to the separation of $ACeO_3$ perovskite phases and conductivity degradation.

Another important group of the IT SOFC electrolytes comprises the materials based on perovskite-type lanthanum gallate, $LaGaO_3$ [25, 26, 46–48, 53, 54, 73, 74]. High oxygen ionic conduction in $LaGaO_3$ can be achieved by substituting lanthanum with alkaline-earth elements and/or

Fig. 2 Temperature dependencies of the total conductivity of solid electrolytes based on ZrO_2 (**a**) [67–70], doped $CeO_{2-\delta}$ (**b**) [6, 71, 72], (La,Sr)(Ga,Mg)$O_{3-\delta}$ [26, 73, 74] and (La,Sr)AlO$_{3-\delta}$ (**c**) [75], and (La,Sr)$_{10}$Si$_6$O$_{27-\delta}$ [76] and the bulk oxygen ionic conductivity of (Gd,Ca)Ti$_2$O$_{7-\delta}$ (**d**) [57]. Data on La$_{0.9}$Sr$_{0.1}$Ga$_{0.8}$Mg$_{0.2}$O$_{3-\delta}$ with 5% Al$_2$O$_3$ addition correspond to $p(O_2)=1$ atm. Data on all other electrolytes correspond to the atmospheric oxygen pressure
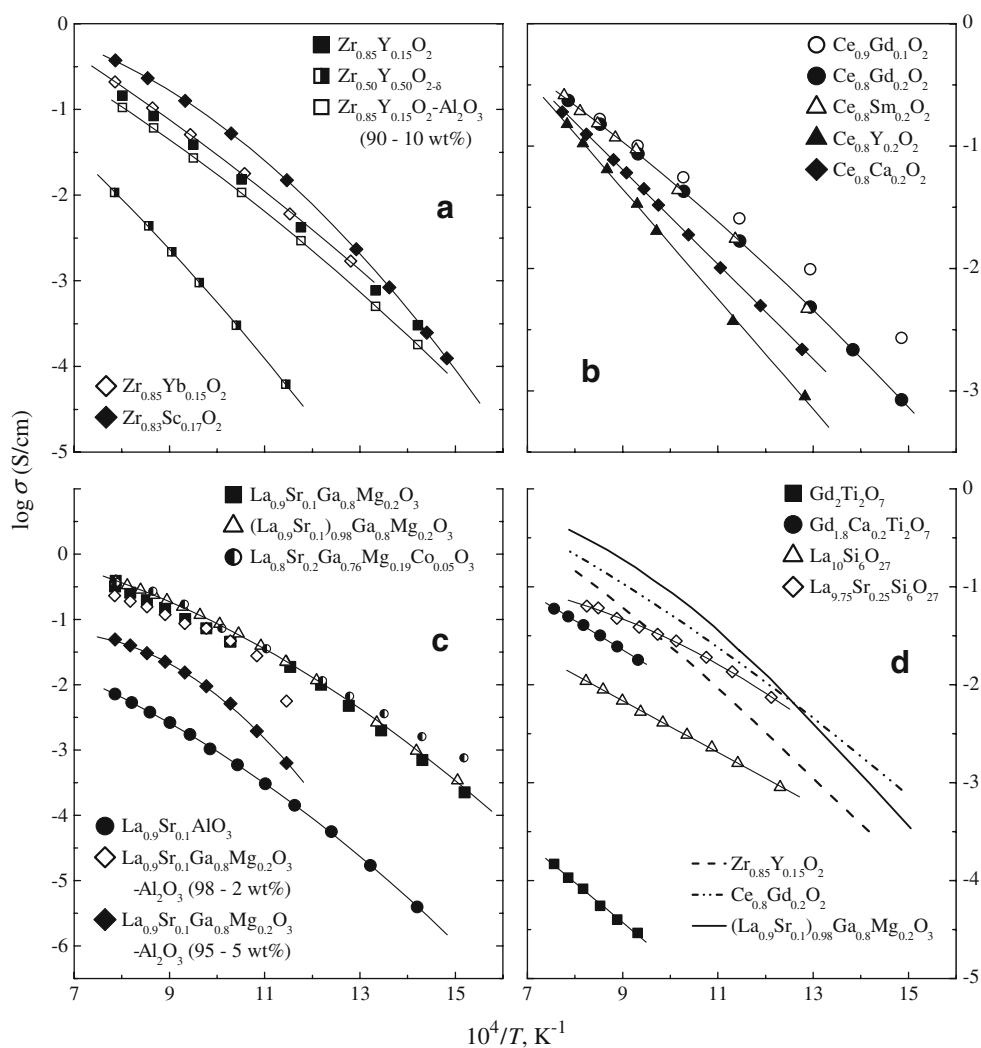
incorporating bivalent metal cations, such as Mg, into the gallium sublattice to increase the oxygen vacancy concentration. Due to the optimum ratio between A- and B-site cation sizes in the ABO_3 perovskite lattice, doping with Sr leads to a higher ionic conductivity in comparison with Ca or Ba [53, 78, 79]. For $La_{1-x}S_xGa_{1-y}Mg_yO_{3-\delta}$ (LSGM) series, the maximum ionic transport is achieved at $x=0.10–0.20$ and $y=0.15–0.20$; further acceptor-type doping results in progressive vacancy ordering. A decrease in the conductivity is also observed if decreasing the average A-site cation radius or creating A-site deficiency. On the contrary, the introduction of small amounts of variable-valence cations, such as cobalt or iron, into the B-sites increases the ionic conduction in LSGM with a moderate influence on the electronic conductivity that still can be neglected [80–82]. The concentration of transition metal dopants should be however limited to 3–7%; further additions lead to undesirable effects, in particular increasing electronic and decreasing ionic transport.

Despite the relatively low ionic conductivity (Fig. 2d), the materials derived from $LnAlO_3$ perovskites and $Gd_2Ti_2O_7$ pyrochlores are still of potential interest, particularly for the anode protective layers and isomorphic additives to composite solid electrolytes [26, 83] due to their low costs. The maximum ionic transport in these systems is observed for $La_{1-x}S_xAlO_{3-\delta}$ at $x≈0.10$ [75] and for $Gd_{2-x}Ca_xTi_2O_{7-\delta}$ at $x≈0.20$ [57].

In the case of $Ln_{10-x}Si_6O_{26\pm\delta}$-based electrolytes with apatite-like structure [58–61, 76], competitive levels of ionic conductivity were achieved for the La-containing compounds with a significant oxygen hyperstoichiometry, 26.2–26.8 oxygen anions per unit formula at temperatures below 900 K (Fig. 2d). Decreasing oxygen concentration below the stoichiometric value leads to the vacancy mechanism becoming dominant and a considerable drop in ionic transport; decreasing Ln^{3+} radius also results in a lower conductivity, as for the perovskite-type compounds.

Electronic conductivity, stability, and thermal expansion

With respect to other SEs, a minimum electronic contribution to total conductivity in the oxygen partial pressure range most important for practical applications, from $10^{-25}–10^{-20}$ atm up to 100–200 atm, is characteristic of stabilized zirconia [6, 16, 33, 39, 47, 61–65, 72, 81–89]. In reducing environments, the n-type electronic transport in ThO_2-, $LaGaO_3$-, and $La_{10-x}Si_6O_{26\pm\delta}$-based electrolytes is lower than that of stabilized ZrO_2, but the performance of silicate and gallate materials at low $p(O_2)$ is limited by reduction, volatilization, and/or surface spreading of silicon and gallium oxides rather than the n-type electronic conductivity (e.g., [61, 73, 84] and references cited). As an example, the oxygen pressure dependencies of total conductivity of LSGM and $La_{10-x}(Si,Al)_6O_{26\pm\delta}$ at reduced $p(O_2)$ are quite complex [61, 73], suggesting the possible decomposition or decrease in the ionic conduction. On the other hand, LSGM-based materials exhibit no essential ageing in the intermediate temperature range [65], which is often critical for zirconia electrolytes. Under oxidizing conditions, the p-type electronic contribution to total conductivity of LSGM is highest compared to the ZrO_2-, $La_{10-x}Si_6O_{26\pm\delta}$-, and CeO_2-based systems [16, 39, 47, 62, 72, 85, 86, 88, 89]; nonetheless, this level of hole conductivity is still acceptable for practical applications. Table 2 lists selected examples of the electron transference numbers in oxidizing atmospheres.

The main problems in using doped ceria as SOFC electrolyte arise from a relatively easy reducibility at low oxygen partial pressures, which leads to increasing n-type electronic transport and possible mechanical failure under large oxygen chemical potential gradients [6, 33, 41, 46–49, 62, 72, 77, 85]. For comparison, at 1073 K the low-p (O_2) electrolytic domain boundary corresponds to the oxygen partial pressure lower than 10^{-30} atm for $La_{0.9}Sr_{0.1}Ga_{0.8}Mg_{0.2}O_{3-\delta}$ (LSGM12) and to approximately 10^{-15}

Table 2 Examples of the electron transference numbers (t_e) and total electronic conductivity (σ_e) of solid-electrolyte ceramics under oxidizing conditions

Composition	T (K)	$p(O_2)$ (atm)	t_e	σ_e (mS/cm)	Ref.
$Zr_{0.9}Y_{0.1}O_{2-\delta}$	1273	0.21	5.0×10^{-5}		[16]
$Zr_{0.9}Sc_{0.1}O_{2-\delta}$	1273	0.21	3.8×10^{-4}		
$Zr_{0.85}Ca_{0.15}O_{2-\delta}$	1273	0.21	8.6×10^{-4}		
$Ce_{0.8}Gd_{0.2}O_{2-\delta}$	873	0.21	6.9×10^{-4}	0.003	[85]
	973	0.21	1.1×10^{-3}	0.015	
	1123	1.0	3.7×10^{-3}	0.42	[72]
$La_{0.9}Sr_{0.1}Ga_{0.8}Mg_{0.2}O_{3-\delta}$	1073	0.21		0.36	[86]
	1073	10^{-3}	1.0×10^{-2}		[73]
$(La_{0.9}Sr_{0.1})_{0.98}Ga_{0.8}Mg_{0.2}O_{3-\delta}$	1073	10^{-3}	4.7×10^{-3}		[73]
$Gd_{1.90}Ca_{0.10}Ti_2O_{7-\delta}$	1073	1.0	0.11	2.1	[57]
	1073	0.21	4.1×10^{-2}	0.487	[87]
$Gd_{1.86}Ca_{0.14}Ti_2O_{7-\delta}$	1073	0.21	3.8×10^{-2}	0.535	[87]
$La_{0.9}Sr_{0.1}AlO_{3-\delta}$	1073	0.21	0.64	1.9	[75]

σ_e and t_e both correspond to the sum of p- and n-type electronic contributions.

atm for $Ce_{0.8}Gd_{0.2}O_{2-\delta}$ (CGO20). The acceptor-type dopant additions further promote reducibility of $Ce(Ln)O_{2-\delta}$; an optimum combination of the ionic conductivity and low-$p(O_2)$ stability was found for compositions with moderate dopant content, such as $Ce_{0.9}Gd_{0.1}O_{2-\delta}$ (CGO10) [33, 49]. Whatever the cation composition, the problems arising from reduction at high temperatures make ceria electrolytes viable only for the intermediate temperature range.

The $(La,Sr)AlO_{3-\delta}$ perovskites and $(Gd,Ca)_2Ti_2O_{7-\delta}$ pyrochlores possess a substantial p-type electronic conductivity under oxidizing conditions [57, 75, 87], but are more stable with respect to reduction and component volatilization in reducing atmospheres if compared with ceria-, gallate-, and silicate-based materials. For example, the electron transference numbers of $Gd_{1.9}Ca_{0.1}Ti_2O_{7-\delta}$ in air are as high as 0.07–0.11 at 1073–1223 K [57]; the ionic contribution to total conductivity of $La_{0.9}Sr_{0.1}AlO_{3-\delta}$ at 873–1173 K is smaller than 40% under O_2/air gradient and higher than 90% under the air/4% H_2 gradient [75].

Table 3 and Fig. 3 compare the typical TEC values of the solid-electrolyte ceramics and perovskite-related mixed conductors, providing a brief guidance for the materials thermomechanical compatibility; detailed analysis of electrochemical and physicochemical properties of mixed-conducting cathodes will be presented in the second part of this review. Most of ZrO_2-, $LaGaO_3$-, $Gd_2Ti_2O_7$-, and $La_{10-x}Si_6O_{26\pm\delta}$ -based electrolytes exhibit similar TECs,
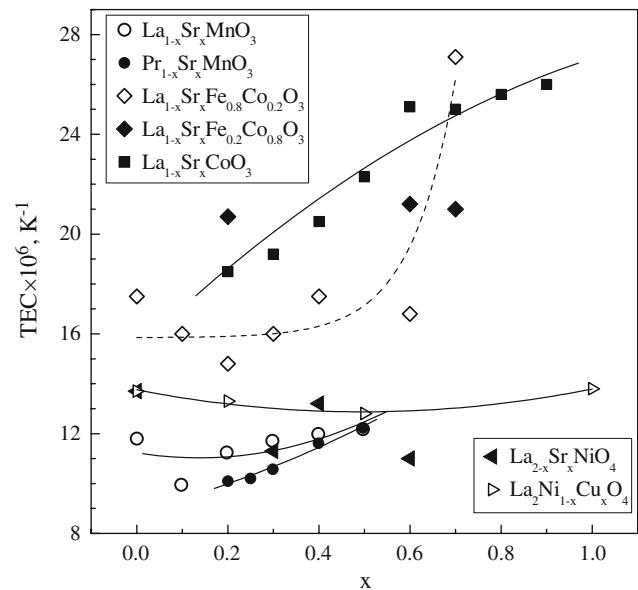

Fig. 3 Average linear TECs of selected perovskite-related cathode materials in air [72, 90, 93–105]

varying in the range $(9–12)\times10^{-6}$ K^{-1}. A moderately higher expansion is observed for doped ceria and for transition metal-containing gallates, thus limiting the possible use of the anode protective layers. The TECs of stabilized zirconia and doped lanthanum gallate can be modified, to some extent, by small additions of silica-scavenging components, such as highly dispersed alumina; these additives make it

Table 3 Average linear thermal expansion coefficients of solid-electrolyte ceramics in air

Composition	T (K)	TEC$\times10^6$ (K^{-1})	Ref.
$Zr_{0.92}Y_{0.08}O_{2-\delta}$	300–1273	10.0	[69]
$Zr_{0.92}Y_{0.08}O_{2-\delta}$ –Al_2O_3 (90–10 wt%)	300–1273	9.7	[69]
$Zr_{0.85}Y_{0.15}O_{2-\delta}$	300–1273	10.9	[90]
$Zr_{0.5}Y_{0.5}O_{2-\delta}$	300–1273	9.4	[16]
$Ce_{0.9}Gd_{0.1}O_{2-\delta}$	773	12.4	[91]
	853	12.5	
$Ce_{0.8}Gd_{0.2}O_{2-\delta}$	773	12.5	
	853	12.6	
	300–1073	12.5	[90]
	300–1273	12.7	
$La_{0.9}Sr_{0.1}Ga_{0.8}Mg_{0.2}O_{3-\delta}$	300–1073	10.4	[26]
	300–1473	11.9	[73]
	300–1073	10.9	[90]
$(La_{0.9}Sr_{0.1})_{0.98}Ga_{0.8}Mg_{0.2}O_{3-\delta}$	300–1473	11.8	[73]
$La_{0.9}Sr_{0.1}Ga_{0.8}Mg_{0.2}O_{3-\delta}$ -Al_2O_3 (95–5wt%)	300–1073	9.9	[26]
$La_{0.9}Sr_{0.1}Ga_{0.76}Mg_{0.19}Co_{0.05}O_{3-\delta}$	300–1473	12.7	[74]
$Gd_2Ti_2O_{7\pm\delta}$	323–1273	10.8	[92]
$Gd_{1.90}Ca_{0.10}Ti_2O_{7-\delta}$	400–1303	10.5	[87]
$Gd_{1.86}Ca_{0.14}Ti_2O_{7-\delta}$	400–1303	10.4	
$La_{9.67}Si_{4.5}Al_{1.5}O_{25.75}$	373–1173	10.0	[89]
$La_{9.83}Si_{4.5}Al_{1.5}O_{26}$	373–1173	8.9	
$La_{9.83}Si_{5.5}Al_{0.5}O_{26.5}$	373–1273	10.8	
$La_{10}Si_5AlO_{26.5}$	473–1173	9.1	

possible to decrease grain-boundary resistance and to improve mechanical strength, which results from retarding grain growth during sintering [26, 106, 107]. The comparison of the data in Fig. 3 and Table 3 shows also that the number of cathode materials compatible with common SEs is essentially limited to the manganite-, nickelate-, and cuprate-based systems and to perovskite-related ferrites with a low concentration of acceptor-type dopants. Although the average TECs of the porous electrode layers can be optimized by SE additions, which also enlarge the electrochemical reaction zone, the use of oxide components having TECs higher than $(15–17)\times10^{-6}$ K^{-1} leads usually to insufficient stability of mixed-conducting electrodes.

Electrode reactions

Cathodic processes

The first kinetic studies of high-temperature electrochemical reactions were focused on metal electrodes in contact with solid oxide electrolytes, primarily YSZ, which are still considered as appropriate model systems [41, 108–118]. However, even for these systems, the electrode reaction mechanisms are complex and modeling results are often ambiguous. This is associated with the fact that the reaction path(s) and the rate-limiting steps are all dependent of numerous factors, including properties of the electrode and electrolyte materials, their morphology, gas phase composition and pressure, and thermal and electrochemical prehistory of the cell [34, 41–43, 108–111, 119, 120]. In the simplest cases, the electrochemical processes are often believed to occur in the vicinity of triple-phase boundary (TPB), the junction of gas, electronically conducting electrode, and solid electrolyte [19, 40–42, 108, 115]; the TPB length is mainly determined by the cell microstructure formed during fabrication. In real systems, however, the reaction zone expands over the electrode and/or electrolyte surfaces [40–42, 108, 116, 119]. As all electrolytes possess nonnegligible electronic conduction, the electrochemically active sites may be located at the gas/SE interface with electronic charge carriers delivered along the electrolyte. Moreover, high cathodic overpotentials may result in a partial reduction of the SE surface and increase of electronic transport, thus promoting oxygen exchange [108]. For the electrodes where molecular oxygen may dissolve in the bulk and/or form surface compounds, oxygen reduction may directly occur at the electrode/electrolyte interface, as shown for O2,Ag|YSZ [41, 116]. Finally, for the mixed-conducting oxide cathodes, the reaction zone spreads onto the gas/electrode interface with transfer of reduced oxygen species along the cathode surface and through electrode bulk [40–42]. The latter

mechanism may cause a necessity to consider another triple-phase boundary between the gas, mixed conductor, and current collector [118], although the corresponding effects are often related to surface spreading of the current collector material, changing electrode microstructure, and exchange mechanisms (e.g., [120]).

The diffusion of molecular oxygen in the gas phase, including pores in the electrode layer, becomes rate-limiting at relatively low oxygen partial pressures. This situation is usually characterized by limiting current and reciprocal polarization resistance both proportional to $p(O_2)$ [108, 121], and can be modeled assuming an ideal binary mixture of O_2 and a diluent gas Y [122] with the effective oxygen diffusion coefficient $D_{O_2}^{eff}$ [21, 121, 123]:

$$D_{O_2}^{eff} = \frac{P_s}{\tau_g} \times \frac{D_{O_2-Y} \times D_{O_2}^K}{D_{O_2-Y} + D_{O_2}^K} \tag{1}$$

where $D_{O_2}^K$ is the Knudsen diffusion coefficient of oxygen, τ_g is the gas-phase tortuosity, and P_s is the porosity. In the case of O2,Pt|YSZ cathodes, the gas-diffusion limitations were discarded down to $p(O_2)\approx10^{-3}$ atm [112, 113]. For $La_{0.6}Sr_{0.4}Fe_{0.8}Co_{0.2}O_{3-\delta}$|CGO10, possible gas diffusion polarization was indicated by changing the shape of the electrode impedance spectra at the oxygen partial pressures lower than approximately 0.1 atm [121]. These effects are, however, critically dependent on the electrode microstructure [42, 124]. For example, numerical simulations [124] showed that, for a composite cathode with 40% porosity and 60% volume fraction of ionically conducting component, diffusion limitations can be expected even in air if the electrode particle size decreases below 0.2–0.3 μm. Hence, enlarging the TPB length via reducing grain size may only be effective on a micron scale; further improvement requires the formation of functionally graded microstructures and the incorporation of nano-sized catalysts.

The concentration polarization-related phenomena are often associated with the slow diffusion of other species. In addition to various surface species involving oxygen, these may include ionic charge carriers (e.g., vacancies) in the electrolyte surface layers, oxygen anions or atoms in the electrode bulk, and electronic charge carriers, especially when the electronic conductivity of the electrode is insufficient [41, 42, 84, 108, 125–127]. The former mechanism may take place, in particular due to highly nonuniform current distribution in the electrolyte and/or to diffusion of variable-valence cations from the cathode into the SE surface where the ionic charge-carrier concentration becomes strongly dependent on the electrode overpotential (η). The effects of nonuniform current density and the relationships between electrode polarization, ohmic potential drop in the solid electrolyte, and cathode microstructure

were examined by Adler [42], Sasaki et al. [125], and Svensson and Nişancioğlu [126]. Models describing oxygen transport in the bulk of dense and porous cathodes can be found in Pelfiryev et al. [41], Adler et al. [121], Liu [122], and Mizusaki et al. [128].

Another complex class of cathodic phenomena is the adsorption and conversion of molecular O_2 into electrochemically active intermediate species. In addition to oxygen ad-atoms and O^{2-} anions, numerous forms of intermediates (O_2^-, O_2^{2-}, O^-, etc.) are often assumed to exist at the electrode surface; in many cases, such hypotheses require further validation [42, 108, 129–131]. Furthermore, the presence of several limiting steps, serial or parallel, may lead to the impossibility to determine the exact state of the oxygen intermediates by the kinetic measurements. As an illustration, Fig. 4 shows two typical combinations of the adsorption/discharge/diffusion steps involving oxygen ad-atoms and O^- sub-ions. The simplest models describing the electrode behavior at low and moderate overpotentials (see, for example, [41, 42, 108–111]) postulate minor deviations from equilibrium between the surface states and gaseous O_2 when the Henry, Langmuir, or Temkin equations can be used for the dissociative adsorption:

$$[O_{ad}] = K \times p(O_2)^{1/2} \tag{2}$$

$$\theta_O \equiv \frac{[O_{ad}]}{[O_{ad}]_{max}} = \frac{K \times p(O_2)^{1/2}}{1 + K \times p(O_2)^{1/2}} \tag{3}$$

$$[O_{ad}] = [O_{ad}]_{max} \times \frac{RT}{\alpha_0} \times \ln \left[\beta_0 \, p(O_2)^{1/2} \right] \tag{4}$$

where $[O_{ad}]$ is the concentration of ad-atoms, K is an equilibrium constant, θ is the relative surface coverage, $[O_{ad}]_{max}$ is the total number of sites available for adsorption, α_0 is the parameter reflecting surface inhomogeneity,
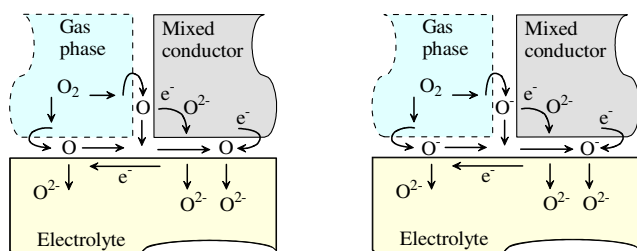

Fig. 4 Examples of the cathode reaction pathway for a porous mixed-conducting electrode with surface diffusion of oxygen ad-atoms (*left*) and O^- sub-ions (*right*)

and β_0 is the adsorption coefficient at the sites with maximum adsorption enthalpy. The elementary adsorption isotherm based on the Henry equation, Eq. 2, may only be valid for a low surface coverage [132]. The Langmuir isotherm, Eq. 3, has a wider applicability range, but presumes a homogeneous adsorbent surface and noninteracting adsorbate species [108, 132, 133]. Notice that for real systems, absolute values of the adsorption enthalpy decrease with increasing surface coverage [132], thus making it necessary to use integral forms of the Langmuir isotherm. The simplified Temkin isotherm, Eq. 4, can be applied for substantially nonuniform surfaces and moderate coverage [108]; a similar approximation was also suggested for binary gas adsorption [132].

The formulae to describe the adsorption-governed oxygen exchange steps are usually based on analogous assumptions. For example, the flux for oxygen chemisorption and dissociation was expressed as [108, 134]:

$$j_{O_2} = j^0_{O_2} \times \left(1 - \theta_O^2\right) \tag{5}$$

where $j^0_{O_2}$ is the exchange flux density. In the conditions when oxygen adsorption is rate-limiting, the electrical current density (i) was defined by [118, 133]:

$$i = 4F \times \left[k_1 \times p(O_2) \times \left(1 - \theta_{O,st}\right)^2 - k'_1 \times \theta_{O,st}^2 \right] \tag{6}$$

where k_1 and k_1' are the constants of forward and backward processes, and $\theta_{O,st}$ is the steady-state coverage. The situation when the adsorption of molecular O_2 is retarding and the subsequent adsorbate dissociation is in virtual equilibrium was formalized assuming [135]:

$$i = 4F \times k_a \, p(O_2) \times (1 - \theta_{O_2} - \theta_O) \tag{7a}$$

$$\theta_{O_2} \times (1 - \theta_{O_2} - \theta_O) = K_d \times \theta_O^2 \tag{7b}$$

where k_a and K_d are the adsorption and equilibrium dissociation constants, respectively. The latter process can also be considered as the dissociation of gaseous O_2 in the immediate proximity to the surface, followed by adsorption of oxygen atoms [136].

The charge-transfer kinetics is commonly analyzed using the classical Butler–Volmer expression [41, 108, 112, 137, 138]:

$$i = i_0 \left[\exp\left(\frac{\alpha z F \eta}{RT}\right) - \exp\left(-\frac{\beta z F \eta}{RT}\right) \right] \tag{8}$$

where i_0 is the exchange current, z is the number of electrons involved in the rate-determining step, and α and β are the transfer coefficients. One should however mention that experimental η–i relationships may apparently follow

the Tafel (or Butler–Volmer) like dependencies if even the interfacial electrochemical kinetic steps are equilibrated [42, 137–139]. This situation may be observed, in particular, when the reaction rate is co-limited by several sorption- and transport-related steps or due to a Nernstian relationship between the applied potential and the activity of electrochemically active species at the electrode surface [42, 139].

The mechanisms with two or more co-limiting steps were initially analyzed for model metal electrodes, such as O_2, Pt|YSZ. In the cases when cathodic reaction is governed by ad-atom diffusion along the electrode/electrolyte interface with charge transfer as the second limiting step, the current density was expressed by the Butler–Volmer type equations [111]:

$$i = \frac{(i_0 \times 2eDc_0)^{1/2}}{\lambda} \left[\exp\left(\frac{3F\eta}{2RT}\right) - \exp\left(-\frac{F\eta}{2RT}\right) \right]$$

(9a)

$$i = \left[\frac{\lambda}{(i_0 \times 2eDc_0)^{1/2}} + \frac{\lambda}{2e\gamma c_0} \exp\left(-\frac{F\eta}{2RT}\right) \right]^{-1}$$

$$\times \left[\exp\left(\frac{3F\eta}{2RT}\right) - \exp\left(-\frac{F\eta}{2RT}\right) \right]$$

(9b)

depending on the boundary conditions. Here, λ is the diffusion length, c_0 is the relative equilibrium concentration of ad-atoms, D is the interfacial diffusion coefficient, and γ is a constant. For the dissociative oxygen adsorption coupled with diffusion along the gas/metal interface (GM), the current per TPB unit length was formulated as [41]:

$$i = i_0^{GM} \left[\exp\left(\frac{6F\eta}{RT}\right) - 3\exp\left(\frac{2F\eta}{RT}\right) + 2 \right]^{1/2}$$
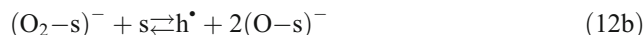
(10)

For the diffusion along the metal/electrolyte interface (ME) and subsequent oxygen incorporation into the SE membrane with constant ion concentration [41]:

$$i = i_0^{ME} \left[\exp\left(\frac{(1+\alpha)F\eta}{RT}\right) - \theta'_O \exp\left(-\frac{\beta F\eta}{RT}\right) \right]$$

(11)

where θ'_O is the ratio of oxygen atom concentration at the GM to its equilibrium value. Equations 10 and 11 were derived assuming that the width of both gas/metal and gas/electrolyte interfaces is much smaller than the corresponding surface-diffusion penetration depths, the oxygen diffusion coefficient in the adsorption layer is concentration-independent, and adsorption obeys the Henry

equation. It should be emphasized that analogous current-overpotential dependencies, involving relative concentrations of oxygen sub-ions or electron-holes instead of θ'_O, can also be obtained for other processes shown in Fig. 4, except for the oxygen transport through electrode bulk [41].

One attractive model for oxygen reduction at the surface of mixed-conducting oxide cathode with p-type electronic transport was considered by Adler et al. [121], assuming the following reaction steps:

$$O_2(gas) + s \rightleftarrows h^\bullet + (O_2-s)^-$$

(12a)

$$(O_2-s)^- + s \rightleftarrows h^\bullet + 2(O-s)^-$$

(12b)

$$(O-s)^- + V_O^{\bullet\bullet} \rightleftarrows h^\bullet + s$$

(12c)

where $h^\bullet$ and s denote electron-holes and active surface sites, respectively. To describe these processes, Adler et al. [121] suggested an equation similar to that for the charge-transfer reactions, irrespective of limiting stage:

$$r = r_0 \left[\exp\left(\frac{\alpha_f}{RT} \Delta\phi_s\right) - \exp\left(\frac{-\alpha_b}{RT} \Delta\phi_s\right) \right]$$

(13)

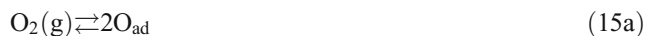where r is the rate of limiting step, r_0 is the so-called neutral flux density of exchange, α_f and α_b are constants depending on specific reaction mechanism, and $\Delta\phi_s = \frac{1}{2}\phi_{O_2}^{gas} + \phi_{V_O}^{MC} - 2\phi_h^{MC}$ is the electrochemical potential difference between reactants and products.

The competing processes of bulk and surface oxygen transport in the mixed-conducting electrodes were analyzed in numerous works (e.g., [108, 115, 121, 122, 126, 128, 137, 140–144] and references cited). Quantitative description of these processes is only possible by numerical modeling; even in the latter case, the formulae for interfacial exchange and surface diffusion are still the subject of serious debates and controversies. As an example of simplified approaches, one may mention the generalized formula [108]:

$$i = C_1 \times C^{1/2}$$

$$\times \left[\frac{a_1 - a_2}{(a_1 + 2b)(a_2 + 2b)} + \frac{\exp((a_1 + 2b)\eta)}{a_1 + 2b} - \frac{\exp((a_1 - 2b)\eta)}{a_2 + 2b} \right]^{1/2}$$

(14)

where $b = \frac{zF}{\nu RT}$, and the electrode electronic conductivity depends on the overpotential as $\sigma_e = C_1 \times \exp\left(\frac{zF\eta}{\nu RT}\right)$ with C_1, ν, and z being constants. In this equation, $a_1 = -b$, $a_2 = (-2F/RT - b)$, $C_2 = 8FD_i \, p(O_2)^{1/m} S \times (C_1 d)^{-1}$ for the regime of limiting ion transport; $C_2 = 4FS \, j_0 \times C_1^{-1}$, $a_1 = (2F/RT - b)$, and $a_2 = -b$ for the adsorption regime; and $C_2 = 8FD_{O_2} \times p(O_2) S \times (C_1 d)^{-1}$, $a_1 = (4F/RT - b)$, and $a_2 = -b$ for the regime of limiting

transport of molecular oxygen. Here, D_i is the effective ion diffusion coefficient independent of $p(O_2)$; d is the effective thickness of the diffusion layer, which is significantly lower with respect to the electrode thickness; the values of the m parameter are determined by the oxygen vacancy formation mechanism under equilibrium conditions; S is the effective surface area where the electrochemical reaction occurs; and j_0 is the exchange flux density. Another model for two serial processes governing electrode kinetics was suggested considering $La_{0.85}Sr_{0.15}MnO_{3-\delta}$ cathodes and the following hypothetical mechanism [145]:

$$O_2(g) \rightleftarrows 2O_{ad} \tag{15a}$$

$$O_{ad} + e^- \rightleftarrows O_{ad}^- \tag{15b}$$

$$O_{ad}^- \rightleftarrows O_{TPB}^- \tag{15c}$$

$$O_{TPB}^- + e^- + V_O^{\bullet\bullet} \rightleftarrows O_{TPB}^{2-} \tag{15d}$$

and two additional pathways with O_{ad}^- formation through $O_{2,ad}^-$ at the electrode surface or at the TPB; the oxygen adsorbates were assumed to diffuse along the electrode surface. For one particular case when the reactions 15b and 15c are rate-determining and other steps are in virtual equilibrium, the current density was expressed as [145]:

$$i = i_{0,2} \times i_{0,3} \times \left[\exp\left(\frac{2F\eta}{RT}\right) - 1 \right]$$
$$\times \left[i_{0,2} \times \exp\left(\frac{F\eta}{RT}\right) + i_{0,3} \times \exp\left(\frac{F\eta}{2RT}\right) \right]^{-1} \tag{16}$$

where $i_{0,2}$ and $i_{0,3}$ are the exchange current densities of the steps 15b and 15c, respectively. When the surface coverage is low, the latter quantities are proportional to $p(O_2)^{3/8}$ and $p(O_2)^{1/4}$, correspondingly.

These equations suggest that when the overall mechanism is relatively simple and parallel reaction paths can be neglected, the rate-determining steps might be discerned analyzing the oxygen partial pressure dependencies of polarization resistance (R_η) or limiting currents (i_{lim}). However, due to the factors listed above, this may only be true for ideal systems with well-defined pattern microstructures. For instance, Table 4 presents several examples of experimentally observed exponent (m') for the power dependencies of R_η and i_{lim} on the oxygen partial pressure [105, 128, 133, 142, 146–154]. Even for similar cathode compositions in contact with zirconia-based electrolytes, these values vary in a wide range, depend on the microstructural parameters, and may lead to serious contradictions. One particular conclusion is that the selection of

SOFC cathode materials cannot be based simply on the comparison of electrochemical performance for electrode layers with different composition, microstructure, and prehistory. This procedure should include, at least, preliminary evaluation of optimum processing conditions for a given family of electrode materials, systematic analysis of the relationships between the composition and electrochemical activity for electrodes with similar microstructures prepared using identical fabrication routes and subsequent microstructural optimization. Also, the identification of the oxygen reduction mechanisms involving porous mixed-conducting cathodes is only possible combining the electrochemical measurements with other techniques, primarily spectroscopic analyses, numerical modeling, and electrode patterning. An analogous conclusion can be drawn when investigating the large variety of impedance spectroscopy results and theoretical approaches developed for their analysis (e.g., [42, 105, 108, 112, 113, 121, 122, 127, 142, 155, 156] and references cited). Whilst the electrochemical impedance spectroscopy is among the most powerful tools for studying electrode performance, the use of relatively simple equivalent circuits to separate electrode signal components and the attribution of definite physical meaning to the circuit elements are always a subject of discussions.

Anodic reactions

The majority of research works focused on the analysis of anodic mechanisms was undertaken using model Ni and Pt metal electrodes in H_2-containing atmospheres (see, for example, [157] and references therein). Nonetheless, the results are relevant for practice because the common anode compositions are based on Ni-YSZ cermets, while both Ni and Pt have excellent catalytic properties in the oxidation reactions occurring at SOFC anodes; nano- and submicron-sized Pt particles are widely used to promote the oxidation and exchange processes. Furthermore, for most anode materials, the electrocatalytic activity for H_2 oxidation is higher than that for CO and CH_4. The performance of SOFCs fueled by hydrocarbon conversion products is, hence, primarily dependent on the partial pressures of H_2 and H_2O. Also, the application of H_2-fueled SOFCs may be advantageous in terms of environmental impact, namely, zero emission of the greenhouse gases.

As for SOFC cathodes, the anodic reaction mechanisms and electrochemical performance depend critically on the electrode microstructure [157–170]; selected examples are presented in Table 5. In the case of anodes, these factors are even more important, particularly due to significant sintering of the electrode particles at elevated temperatures and/ or under high current densities [41, 108, 162, 168]. The key polarization characteristics observed for porous anode

Table 4 Approximate exponent values of the $p(O_2)$-dependencies of polarization resistance for various oxide cathodes in contact with solid electrolytes based on zirconia, ceria, and lanthanum gallate

Electrode composition	Cathode type	T (K)	$p(O_2)$ (atm)	m'	Ref.
$La_{1-x}S_xMnO_3$	Point	1233	10^{-5}–1	1/2	[142]
(x=0.1–0.4)	Point, after high cathodic polarization	1233	10^{-5}–1	3/8	[142]
$(La_{0.82}Sr_{0.18})_{0.82}MnO_3$	Porous	1123–1273	10^{-2}–0.21	0.45–0.86	[146]
$La_{0.85}Sr_{0.15}MnO_3$	Porous	1073–1170	10^{-3}–1	1/4[a], 1[b]	[147]
$La_{0.8}Sr_{0.2}MnO_3$	Porous	1073–1273	<10^{-3}	1	[148]
	Porous	1073–1273	10^{-3}–1	1/2	[148]
$La_{0.8}Sr_{0.2}MnO_3$	Porous	823–1073	10^{-3}–1	1/6	[149]
$La_{1-x}S_xMnO_3$	Porous	1073	10^{-2}–0.5	3/4	[150]
(x=0.3–0.7)					
$La_{0.63}Sr_{0.27}MnO_3$	Dense	973–1173	10^{-3}–1	<0	[128]
$La_{0.81}Sr_{0.09}MnO_3$	Dense	1073	10^{-3}–1	0	[133]
$SrMnO_3$	Porous	1073	10^{-2}–0.5	1/2	[150]
$La_{0.6}Ca_{0.4}MnO_3$	Porous	>1173	<10^{-3}	1	[151]
	Porous	973–1173	10^{-3}–1	1/2	[151]
$La_{0.6}Ca_{0.4}MnO_3$	Porous	1073	6×10^{-4}–1	1/3	[152]
$La_{1-x}S_xCoO_3$	Porous	873–1073	10^{-2}–0.5	1/4	[150]
(x=0–0.7)					
$La_{0.6}Sr_{0.4}CoO_3$	Dense	1073	10^{-4}–1	1/2[a]	[133]
$Sm_{0.5}Sr_{0.5}CoO_3$	Dense	1073	10^{-4}–1	1/2[a]	[153]
$La_{1-x}S_xCoO_3$	Porous	1023	10^{-2}–1	0.2–0.4[a]	[154]
(x=0.2–0.4)					
$La_{1-x}S_xFeO_3$	Porous	1073	10^{-2}–0.5	3/4	[150]
(x=0.3–0.7)					
$La_{0.6}Sr_{0.4}FeO_3$	Porous	1073	2×10^{-4}–1	0.17	[152]
$La_2Ni_{0.8}Cu_{0.2}O_4$	Porous	1073	2×10^{-2}–0.21	1/3[b]	[105]
$La_{1.9}Sr_{0.1}CuO_4$	Porous	1073	10^{-3}–1	0.08	[152]
$La_{0.7}Sr_{0.3}CrO_3$	Porous	1073	10^{-2}–0.5	1/2	[150]

[a] Intermediate-frequency contributions in the impedance spectra.
[b] Low-frequency contributions in the impedance spectra.
[c] Ceria-based solid electrolytes.
[d] Lanthanum gallate-based solid electrolytes.

structures are essentially different from those for the model point- and pattern-type electrodes. Another critical issue relates to carbon deposition caused by hydrocarbon pyrolysis and Boudouard reactions (e.g., [171, 172]). Although these processes can be partly suppressed by optimizing the operation temperature and pressure, by increasing current density and/or steam and CO_2 content in the fuel gas, and by catalytic additives [172–178], even

the deposition of small amounts of carbon may lead to irreversible microstructural changes.

If compared to the cathodic processes, the limiting effects of gas diffusion in porous anodes become considerably higher; the counter-diffusion of reactant(s) and product(s) should be necessarily taken into account. Moreover, the difference in opposite mass flows may result in the net mass transport in one direction [123, 179]. In the

Table 5 Examples of experimentally observed exponents of the polarization resistance vs $p(H_2)^{n'}$ and $p(H_2O)^{n''}$ dependencies for Pt- and Ni-based anodes in contact with yttria-stabilized zirconia

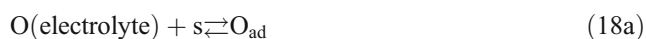| Electrode material	Anode type	T (K)	n'	n''	Ref.
Pt	Porous	973–1073	−1/4 to 1/4	−1/2 to −1/4	[110,159]
Ni	Point	1248	−1/2 to 1/2	−1/2	[161]
	Pattern	973–1073	0	<0	[162]
		1123	0 to 1/2	<0	[162]
		973	−0.24 to −0.11	−0.67 to −0.32	[163]
Ni-YSZ	Porous (fine cermet)	1273	−3/20 to 0	−1/5 to −3/10	[164]
	Porous (coarse cermet)	1273	−1/20	−2/5	[159]
	Porous	1023–1273	Approximately 0		[165]
Ni–yttria-doped TZP[a]	Porous	1123–1273		−1	[166]
	Porous	1123–1273	−1/10	−1/2	[167]

[a] TZP is the so-called tetragonal zirconia polycrystal where the yttria content is lower than necessary for stabilization of the cubic fluorite-type phase.

framework of the mean transport pore model [180], assuming an isotropic porous medium with cylindrical capillary pores, the isothermal gas diffusion in a multicomponent gas mixture can be described in terms the modified Maxwell–Stefan equation and Knudsen diffusion [180, 181]. The diffusion flux is defined by the dusty gas model in a similar way [128]. The simplified expression for the steady-state net diffusion flux of a binary gas mixture (j) may be written as [181]:

$$j = \frac{P_s\, c_{total}\, D_{XY}}{\tau_g\, L}$$

$$\times \ln\left(\frac{D_{XY} + K_X\, r_p}{D_{XY} + K_X\, r_p \times M_X^{1/2} M_Y^{-1/2}}\right) \qquad (17)$$

where c_{total} is the total molar concentration of the gas mixture, L is the thickness, $K_X = \frac{2}{3} \times \left(\frac{8RT}{\pi M_X}\right)^{1/2}$ is the Knudsen number of the component X, r_p is the average pore radius, and M_X and M_Y are the molecular weights of X and Y species, respectively. The net permeation fluxes are contributed by the Knudsen flow, the slip flow at the wall, and the viscous flow [181]. As an example, for H_2–H_2O mixtures in Ni-YSZ cermet with 30% porosity, the effective diffusion coefficient was estimated as 10^{-2} to 10^{-1} cm^2/s at 1273 K [182]; the average free path of a molecule is approximately 0.1 μm. The analysis of concentration and activation polarization of the electrolyte-supporting Ni-YSZ anodes exposed to humidified H_2 indicates that the performance is limited by the gas transport through porous electrode [21]; the effective binary gas diffusion coefficient is 0.1–0.2 cm^2/s at 923–1073 K, increasing on heating. Notice that the gas diffusion-related polarization effects are, again, critically dependent on the electrode microstructure [179].

The hydrogen oxidation mechanisms are essentially similar for bare Ni and for Ni-YSZ composite anodes [160]. One simplified model for H_2 oxidation kinetics on Ni-YSZ cermets [183] was developed on the basis of a continuously stirred tank reactor approach, assuming that the charge transfer and surface diffusion of adsorbates are not rate-determining when the polarization is low. Taking into account several elementary steps

$$O(\text{electrolyte}) + s \rightleftarrows O_{ad} \qquad (18a)$$

$$H_{ad} + O_{ad} \rightleftarrows OH_{ad} + s \qquad (18b)$$

$$H_{ad} + OH_{ad} \rightleftarrows H_2O_{ad} + s \qquad (18c)$$

$$H_2O_{ad} \rightleftarrows H_2O(\text{gas}) + s \qquad (18d)$$

$$H_2(\text{gas}) + 2s \rightleftarrows 2H_{ad} \qquad (18e)$$

the relationships between anodic current and overpotential dependent on O_{ad} coverage were expressed by [183]:

$$\eta = \frac{RT}{2F} \times \ln\left(1 + \frac{i \times f \times K_a}{i \times S + 2F \times x_{H_2O} \times f}\right) \qquad (19)$$

where f is the gas flow rate, K_a is determined by the equilibrium constant of Eq. 18d and rate constants of the backward reactions 18c and 18d, x_{H_2O} is the inlet mole fraction of water vapor, and S is the anode surface area. The materials with larger equilibrium O_{ad} coverage were predicted to exhibit smaller overpotentials [183].

The relevance of concentration polarization for Ni-YSZ anodes was stressed in Wilford et al. [170] and Eguchi et al. [182]. An important particular situation, namely, the coverage-dependent diffusion limitations at high current densities, was considered in Wilford et al. [170]; the hypothesis on slow surface diffusion of hydrogen adsorbed dissociatively at the metal or electrolyte surface is in agreement with the characteristic diffusion times, longer than the residence of OH^- and H_2O adsorbates. The competing adsorption of reactants and products was described using the Langmuir isotherm [170]:

$$\theta_i = \frac{K_i \times p_i}{1 + \sum_i K_i \times p_i} \qquad (20)$$

where p_i is the partial pressure of species i. Another interesting approach for the modeling of (H_2–H_2O), Ni|YSZ pattern anode [184] was based on the assumptions that: (1) electrochemical reactions occur predominantly at the Ni metal surface and directly at the TPB, (2) adsorption of H_2 and H_2O has a nonactivated character, (3) surface diffusion is fast, and (4) gas phase limitations can be neglected and H_2O molecules are involved in two surface reactions, namely, Eq. 18c and $H_2O_{ad} + O_{ad} \rightleftarrows 2OH_{ad}$. On the contrary, Ihara et al. [165] assumed that the rate-determining step is the reaction of two H atoms adsorbed on nickel and one O ad-atom at the YSZ surface. As for Bieberle et al. [184], however, the theoretical current dependencies on H_2 and H_2O partial pressures, calculated using the Langmuir isotherm, may only provide a qualitative description of experimental data [165].

The analysis of Ni-YSZ anode polarization curves in H_2-containing atmospheres, based on a Nernst-type relationship for the concentration and an empirical Butler–Volmer type rate equation, suggested that the reaction is dominated by two steps, one being the charge-transfer reaction affected by $p(H_2O)$ and $p(H_2)$ [167]. The same conclusion was

drawn from the impedance spectra [185]. The presence of YSZ in the cermet was found important for the anode microstructure and total reaction rate, but has no essential influence on the mechanism [185]. On the other hand, due to the ionic conduction in the YSZ network, the active thickness of Ni-YSZ anodes may achieve approximately 10 μm for a layer with fine microstructure [159]. The maximum performance of Ni-YSZ (50–50 vol.%) at 1123–1273 K was observed when the water vapor content in H_2–H_2O gas mixtures was approximately 14% [167]. Accordingly, at temperatures below 1120 K the rate-determining step was identified as the oxidation of hydrogen atoms on the Ni surface [186]. Increasing temperature leads to faster charge-transfer kinetics; then an additional reaction step, possibly adsorption, becomes relevant. For a stripe pattern Ni electrode, the rate-determining steps may include either dissociative adsorption of hydrogen or surface diffusion of the adsorbed reactants [162]. In the case of porous Pt, two processes were suggested as limiting, depending on the oxygen activity (a_O^*) at the YSZ surface near TPB [114]. The first reaction, at $a_O^* > 10^{-10}$, can be expressed by Eq. 18c with the rate equation

$$i = k_2\, \theta_H(Pt)^{1/2}\, \theta_{OH}(YSZ)^{1/2}$$
$$- k''_2\, \theta_{H_2O}(Pt)^{1/2}\, \theta_s(YSZ)^{1/2} \tag{21}$$

The second process governing electrode kinetics at $a_O^* < 10^{-12}$ was formulated as:

$$H_{ad}(Pt) + H_2O_{ad}(YSZ) \rightarrow H_2O_{ad}(Pt) + H_{ad}(YSZ) \tag{22}$$
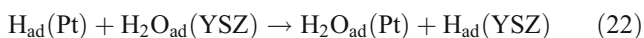
$$i = k_2\, \theta_H(Pt)^{1/2}\, \theta_{H_2O}(YSZ)^{1/2}$$
$$- k'_2\, \theta_{H_2O}(Pt)^{1/2}\, \theta_H(YSZ)^{1/2} \tag{23}$$

Equations 21, 22, and 23 were obtained assuming a Langmuir-type adsorption and predominant roles of H_{ad} adsorbates on the Pt surface and OH_{ad} radicals at the YSZ surface [114].

The electrochemical activity of metal, cermet, and oxide electrodes in the CO–CO_2 atmospheres is substantially worse compared to H_2-containing gas mixtures [8, 41, 122, 162]. Typical examples are presented in Fig. 5. For CO oxidation on porous Pt electrode, the overall rate was suggested to be determined by the chemical reactions involving adsorbed species at the Pt and YSZ surfaces [188]:
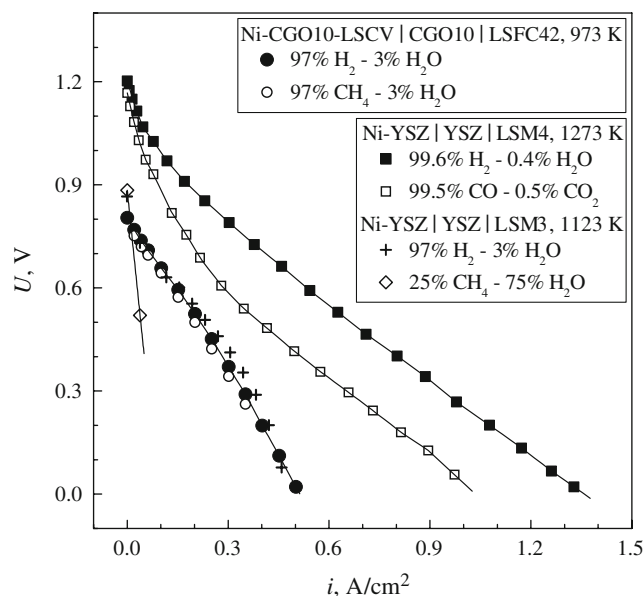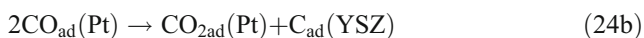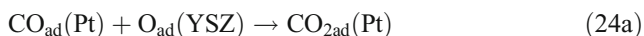
$$CO_{ad}(Pt) + O_{ad}(YSZ) \rightarrow CO_{2ad}(Pt) \tag{24a}$$

$$2CO_{ad}(Pt) \rightarrow CO_{2ad}(Pt) + C_{ad}(YSZ) \tag{24b}$$

Fig. 5 Current–voltage dependencies of model SOFCs with zirconia- and ceria-based solid electrolytes [8, 28, 187]. LSM3 and LSM4 denote $La_{1-x}S_xMnO_{3-\delta}$ with $x=0.3$ and $x=0.4$, respectively. All other abbreviations are explained in the caption of Fig. 1

with the rate equations:

$$i = k_1\, p(CO)^{1/2} \left[a_O^*\right]^{1/2} - k'_1\, p(CO_2)^{1/2} \tag{25}$$

$$i = k_2\, p(CO) - k'_2\, p(CO_2)^{1/2} \left[a_O^*\right]^{-1/2} \tag{26}$$

where the role of the Boudouard process becomes critical in CO-rich atmospheres. The situation when the reaction zone expands along the electrolyte surface was considered assuming fast sorption kinetics and direct oxidation of carbon monoxide [41]:

$$O^{2-} + CO \rightleftarrows CO_2 + 2e^- \tag{27}$$

In the latter case, the current density per TPB unit length can be expressed as [41]:

$$i = i_0^{ME} \left[\theta_e \exp\left(\frac{\alpha F \eta}{2RT}\right) - \exp\left(-\frac{(1+\beta)F\eta}{2RT}\right) \right] \tag{28}$$

where θ_e is the concentration of electronic charge carriers at the TPB. For a mixed-conducting anode in CO–CO_2 atmospheres, a generalized equation similar to Eq. 14 was derived [108]. In this equation, $C_2 = 2S \times i_0/C_1$, $a_1 = -b$, and $a_2 = -(2F/RT + b)$ when the adsorption or diffusion of CO molecules is impeded.

The electrochemical oxidation of CH_4 is characterized, again, by slower kinetics with respect to CO and H_2 due to a fairly high stability of methane molecules and, often, partial deactivation of anodes because of coking [41, 175, 142]. For example, the power densities of cathode-

supported LSM|CYO|YSZ|CYO|Ni-YSZ cells fueled by wet methane are approximately 20% lower compared to humidified hydrogen owing to higher anode resistance [24, 173]. The likely reaction mechanisms include CH_4 reforming with the steam produced by hydrogen oxidation at the TPB, and methane cracking followed by the electrochemical oxidation of hydrogen and carbon [171, 174, 175]. At intermediate temperatures, a higher role of CH_4 oxidative coupling may also be expected due to the kinetic factors [8, 189]. An optimum $p(H_2O)/p(CH_4)$ ratio to maximize the reforming rate was estimated as 0.25–0.50; to avoid carbon deposition, this value should be higher than 0.15 [172]. The anodic polarization may lead to modification of the electrode catalytic activity (so-called NEMCA effect), in particular to an enhanced reforming rate and suppressed coking [172]. For the latter purpose, however, the incorporation of catalytically active additives, such as Ce- and Mo-containing compounds, into cermet compositions seems more effective [41, 45, 72, 171, 178, 190]. A comprehensive analysis of thermodynamic factors and catalytic processes relevant to the anodic oxidation of light hydrocarbons can be found in the Fuel Cell Handbook [1], Alcaide et al. [9], Yano et al. [12], Yentekakis et al. [172], Diskin et al. [177], Peña et al. [190], and York et al. [191].

Effects of ionic transport in electrode materials

The introduction of oxygen ion-conducting materials into the SOFC electrodes often results in a spatial expansion of the electrochemical reaction zone along the electrode/gas and electrode/electrolyte interfaces, thus reducing polarization. As mentioned above, both the electrochemical reaction mechanism and rate may depend directly on the electrode ionic conductivity, which influences the relative roles of adsorption/desorption, charge and mass transfer in the electrode bulk and along the surface [40–42, 108, 122, 141]. However, due to the complexity of electrode processes, no linear correlations between the bulk ionic conduction and electrochemical activity of porous electrodes are often observed [18, 172, 192].

For mixed-conducting cathode layers, at least four competing reaction paths can be easily identified (Fig. 4), leading to the impossibility of a generalized analytical description. Nevertheless, numerous model approaches known in the literature [41, 42, 118, 121, 122, 126, 128, 136, 137, 140–148, 153–156] make it possible to understand particular aspects of the cathodic processes and, in many cases, to predict electrode behavior. Among the relevant examples, one should mention the continuum mass-transport model [143] to describe the competition between the surface and bulk pathways, predicting a critical role of the vacancy concentration for commonly used

perovskite-type mixed conductors. The results seem to be in good agreement with experimental data on $La_{1-x}S_xMnO_{3-\delta}$ cathodes [193]. The numerical finite element calculations [140, 141] showed that, for many conventional mixed conductors, the reaction path involving bulk ion transport is rather unlikely with respect to the surface diffusion. An opposite situation is however observed in the case of significant oxygen-exchange limitations at the electrode surface when the reaction zone may expand into the entire electrode/electrolyte interface [140, 141]. As an example, for porous $La_{0.6}Ca_{0.4}Fe_{0.8}Co_{0.2}O_{3-\delta}$ | $Ce_{0.9}Sm_{0.1}O_{2-\delta}$ cathode with a relatively high level of ionic conduction, the electrode kinetics is influenced by both surface exchange rate and bulk diffusion [121]. For materials exhibiting fast ionic transport, such as $(La,Sr)(Co,Ni)O_{3-\delta}$ or $(La,Sr)(Co,Fe)O_{3-\delta}$ [40, 121], the oxygen penetration depth may reach a few microns; the thickness of electrochemically active layer in porous mixed-conducting cathodes typically decreases with increasing exchange rate and with decreasing ambipolar conductivity [122]. Numerous experimental results on the oxygen surface-exchange and diffusion coefficients, ionic conductivity, and oxygen permeability for a variety of oxide mixed conductors were analyzed in the literature [40, 51, 194–205]. Figure 6 compares the performance of several electrode materials with different levels of bulk ionic transport; representative data on the oxygen ionic conductivity (σ_O) are summarized in Table 6.

The literature data [23, 25, 35, 72, 123, 133, 136, 150, 153, 154, 195, 207, 208] confirm that when comparing large families of oxide cathode materials, the general correlation between electrochemical activity and oxygen
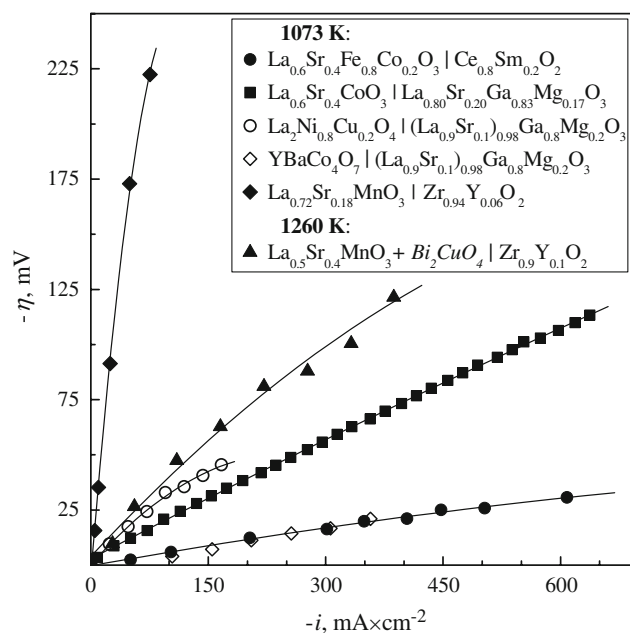
Fig. 6 Comparison of the cathodic overpotentials of oxide electrodes with different levels of mixed conductivity in air [30, 35, 105, 199, 200]

Table 6 Oxygen ionic conductivity of oxide materials in air

Composition	T (K)	σ_O (S/cm)	Ref.
$La_{0.95}Sr_{0.05}MnO_{3\pm\delta}$	1173	1.1×10^{-7}	[201]
$La_{0.90}Sr_{0.10}MnO_{3\pm\delta}$	1273	2.1×10^{-6}	[201]
$La_{0.80}Sr_{0.20}MnO_{3\pm\delta}$	1173	5.9×10^{-7}	[201]
	1273	5.8×10^{-6}	
$La_{0.79}Sr_{0.20}MnO_{3\pm\delta}$	1273	8×10^{-6}	[144]
$La_{0.65}Sr_{0.30}MnO_{3\pm\delta}$	1073	1.7×10^{-4}	[202]
$Pr_{0.65}Sr_{0.30}MnO_{3\pm\delta}$	1073	3.4×10^{-4}	[202]
$La_{0.70}Ba_{0.30}CoO_{3-\delta}$	1273	3.0×10^{-2}	[203]
$La_{0.60}Sr_{0.40}FeO_{3-\delta}$	1073	5.6×10^{-3}	[202]
$La_{0.60}Sr_{0.40}CoO_{3-\delta}$	1073	0.22	[202]
	1105	0.37	[204]
$La_{0.50}Sr_{0.50}CoO_{3-\delta}$	1073	9.3×10^{-2}	[202]
$La_{0.30}Sr_{0.70}CoO_{3-\delta}$	1073	0.76	[202]
	1105	0.75	[204]
$La_{0.20}Sr_{0.80}CoO_{3-\delta}$	1105	0.51	[204]
$SrCoO_{3-\delta}$	1105	0.35	[204]
$La_{0.75}Sr_{0.20}Mn_{0.8}Co_{0.2}O_{3-\delta}$	1073	3.1×10^{-5}	[202]
$Pr_{0.75}Sr_{0.20}Mn_{0.8}Co_{0.2}O_{3-\delta}$	1073	1.1×10^{-4}	[202]
$La_{0.8}Sr_{0.2}Fe_{0.9}Co_{0.1}O_{3-\delta}$	1073	2.2×10^{-3}	[202]
$La_{0.8}Sr_{0.2}Fe_{0.8}Co_{0.2}O_{3-\delta}$	1073	2.3×10^{-3}	[202]
$Pr_{0.8}Sr_{0.2}Fe_{0.8}Co_{0.2}O_{3-\delta}$	1073	1.5×10^{-3}	[202]
$La_{0.8}Sr_{0.2}Fe_{0.2}Co_{0.8}O_{3-\delta}$	1073	4×10^{-2}	[202]
$La_{0.65}Sr_{0.30}Fe_{0.8}Co_{0.2}O_{3-\delta}$	1073	4×10^{-3}	[202]
$La_{0.6}Sr_{0.4}Fe_{0.8}Co_{0.2}O_{3-\delta}$	1073	8×10^{-3}	[202]
$La_{0.6}Sr_{0.4}Fe_{0.2}Co_{0.8}O_{3-\delta}$	1073	5.8×10^{-2}	[202]
$La_{0.6}Sr_{0.4}Fe_{0.2}Co_{0.8}O_{3-\delta}$	1173	0.2	[205]
$YBaCo_4O_{7\pm\delta}$	1073	2.1×10^{-3}	[199]
	1173	9.4×10^{-3}	
	1223	1.1×10^{-2}	
$Y_{0.8}Ca_{0.2}Co_{0.7}Fe_{0.3}O_{3-\delta}$	923	2.4×10^{-6}	[206]
	973	8.3×10^{-6}	
	1023	2.0×10^{-5}	
$La_2Zr_2O_7$	1273	10^{-4}	[104]

diffusivity may be indeed revealed. Moreover, similar correlations exist within the compositional systems characterized by a low ionic conduction, such as LSM where the reaction is essentially localized at the electrode surface; these effects seem associated with a great contribution, which can be provided by even a small enlargement of the electrochemical reaction zone along the electrode/electrolyte interface. For the cathode materials with relatively high ionic conductivity, the role of surface-related processes remains still important, but the electrochemical performance does not correlate directly with the variations in σ_O values induced by moderate doping. Several typical examples are listed below; a more detailed analysis of the relationships between the electrode composition, bulk transport properties, and polarization resistance will be presented in the second part of this review.

The studies of $La(Sr)MnO_{3-\delta}$, $La(Sr)CrO_{3-\delta}$, $La(Sr)FeO_{3-\delta}$, $(La,Sr)(Co,Fe)O_{3-\delta}$, $La(Fe,Ni)O_{3-\delta}$, and $La(Sr)CoO_{3-\delta}$ cathodes in contact with CeO_2-, $LaGaO_3$-, and

ZrO_2-based solid electrolytes demonstrated a maximum activity for the latter three perovskite systems [25, 35, 72, 133, 136, 195], although the thermomechanical stability of cobaltite-based electrodes in such electrochemical cells is insufficient (Table 3 and Fig. 3). In the case of LSM, the rate-determining steps in the intermediate-temperature range include dissociative adsorption and surface diffusion [35]. For $(La,Sr)(Co,Fe)O_{3-\delta}$ and $La(Sr)CoO_{3-\delta}$, the polarization is also contributed by processes at the electrode surface and may often be decreased by increasing the specific surface area [27, 35, 195, 208]. For $La_{1-x}S_xBO_3$ (B=Cr, Mn, Fe, Co) layers sputtered onto YSZ ceramics, the rate-determining steps at temperatures below 1073 K were identified as charge transfer for cobaltites, molecular oxygen dissociation on the surfaces of ferrite and manganite cathodes, and oxygen diffusion along the surface of $(La,Sr)CrO_3$ [150]. The performance of the sputtered electrodes was found to increase in the sequence Cr<Fe<Mn<Co [150]. At the same time, the cathodic reaction mechanism on dense LSM differs considerably from those on porous layers (e.g., [128] and Table 4). In particular, the polarization of porous $(La,Sr)MnO_{3-\delta}$ is drastically reduced by Sr doping, which has no essential effect in the case of dense films [207].

Another necessary comment is that the oxygen surface exchange and charge-transfer processes occurring at the gas/cathode and cathode/electrolyte interfaces, respectively, are usually inter-correlated. This originates, in particular, from the well-known correlation between equilibrium ionic conductivity and exchange parameters [195] and from the effects of ionic charge carrier concentration on the interfacial exchange rate [209, 210]. The nature of contact between the mixed conductor and electrolyte is also of key importance, especially when blocking layers may form and/or significant cation interdiffusion occurs [2, 3, 16, 18, 41–43, 72, 84, 122, 211, 212]. In other words, the reaction kinetics is determined by both bulk and interface properties of the cell components and their interaction.

The conventional SOFC anode materials are based on the cermets comprising, at least, one electronically conducting metal and one oxide phase with oxygen ionic or mixed conductivity. In addition to the reaction zone expansion, oxide components have also a number of other important functions, namely, matching thermal expansion of the cell components, preventing sintering of metal particles, stabilizing the anode layer with respect to redox cycling, and acting as catalyst or catalyst support. Consequently, it is often impossible to separate the effects originating from ionic conduction in the oxide phase from changes in the catalytic behavior and anode microstructure. In the case of Ni-YSZ cermets, stabilized zirconia additions were reported to improve the fuel oxidation kinetics without essential influence on the reaction mechanism and

to enable the formation of well-developed morphology, whilst the electrochemically active zone expands up to 10–20 μm from the electrolyte surface due to ionic transport in the zirconia matrix [159, 160, 164, 185]. No significant sintering of yttria-stabilized zirconia was observed in Ni-YSZ after 4000 h at 1273 K [213]. The high-frequency response in the impedance spectra of such anodes was attributed to the charge-transfer process from Ni to YSZ in combination with the ionic resistivity of YSZ grains [164]. On the other hand, the use of $Zr_{0.94}Y_{0.06}O_2$ instead of $Zr_{0.85}Y_{0.15}O_2$ decreases slightly the polarization of Ni-YSZ cermets with comparable microstructures (Fig. 7), despite the lower conductivity of partially stabilized zirconia. The incorporation of ceria-based phases with a high catalytic activity enhances the performance of anode materials [5, 37, 38, 72, 214–219]; selected examples are presented in Fig. 8. The use of acceptor-doped cerium dioxide, which exhibits a significant mixed ionic–electronic conductivity under reducing conditions [49, 72], appears even advantageous with respect to undoped $CeO_{2-\delta}$ [214]. However, the polarization resistance of Ni-CGO is higher than that of Ni-YSZ cermets with the same volume fraction of nickel [222], particularly owing to the insufficient thermomechanical stability of the former anode materials. One likely reason relates to extensive volume changes induced by the variations of oxygen chemical potential and/or current; excessively large concentrations of ceria-based components in the cermets may, therefore, have an unfavorable effect. As oxygen stoichiometry of the zirconia-based solid electrolytes is essentially constant under the SOFC operation conditions, a relatively high electrochemical performance can be achieved combining metallic Ni, YSZ, and

ceria-containing phases [219, 221]. In principle, further improvement may be expected on the replacement of YSZ, which stabilizes the electrode microstructure with respect to redox cycling and Ni sintering, by alternative redox-stable components having a higher electrocatalytic activity and ionic conductivity.

Although the fluorite-like ceria solid solutions might be, in theory, used as anode materials without any metallic additives [216], the presence of metallic phase seems still necessary to provide a sufficient level of electronic transport. The total electrical conductivity of doped ceria is several orders of magnitude lower than that of metals, such as Ni and Cu, even in strongly reducing atmospheres [41, 49, 77, 85, 223]. As a result, the polarization of ceria-based ceramic anode layers is considerably higher if compared to cermets containing the same oxide phases [222]; dispersion of minor amounts (1–3 wt%) of nickel onto the surface of mixed-conducting oxide anodes reduces the overpotentials [222]. This situation is quite typical for oxide electrode materials where the total conductivity under operation conditions is lower than 50–100 S/cm (e.g., [127]). At the same time, comparative studies of the anode materials with different levels of the oxygen ionic transport, namely, $Ni-Zr_{0.85}Y_{0.15}O_{1.93}$, $Ni-Ce_{0.9}Gd_{0.1}O_{2-\delta}$, $Ce_{0.6}Gd_{0.4}O_{2-\delta}$, $La_{0.75}Sr_{0.25}Cr_{0.97}V_{0.03}O_{3-\delta}$, and $Zr_{0.71}Y_{0.12}Ti_{0.17}O_{2-\delta}$, confirmed that increasing ionic conductivity leads to lower values of the total polarization resistance [222]. An analogous correlation was found between the anodic overpotentials and ionic conduction in the cermet layers made of 5 wt% $Ni-Ce_{0.8}Sm_{0.2}O_{2-\delta}$, $Ni-Ce_{0.8}Gd_{0.2}O_{2-\delta}$, $Ni-Nd_{0.9}Ca_{0.1}Ga_{0.9}Co_{0.1}O_{3-\delta}$, $Ni-La_{0.9}Sr_{0.1}Ga_{0.8}Mg_{0.115}Co_{0.085}O_{3-\delta}$, $Ni-Gd_2Ti_2O_7$, and pure Ni [37].

Electrolyte surface- and current collection-related factors

The partial ionic and electronic conductivities of solid-electrolyte material are relevant not only to the ohmic losses and leakage currents in SOFCs, but may also influence the electrochemical processes (see, e.g., [224–226]). First of all, the electrode polarization resistance usually increases with the electrolyte resistivity [38, 118, 224, 226–228], as illustrated by Fig. 9. These relationships can be theoretically explained by the nonuniform electrode theory [118] as a result of local variations in R_η due to discrete contacts between the porous electrode and dense electrolyte. The effect of ionic current distribution at the electrolyte surface on the population of active sites for oxygen incorporation was noted in Horita et al. [229]. Regardless of the possible variations in the current density, the overall exchange rate is always dependent of the ionic and electronic charge-carrier concentrations and mobilities
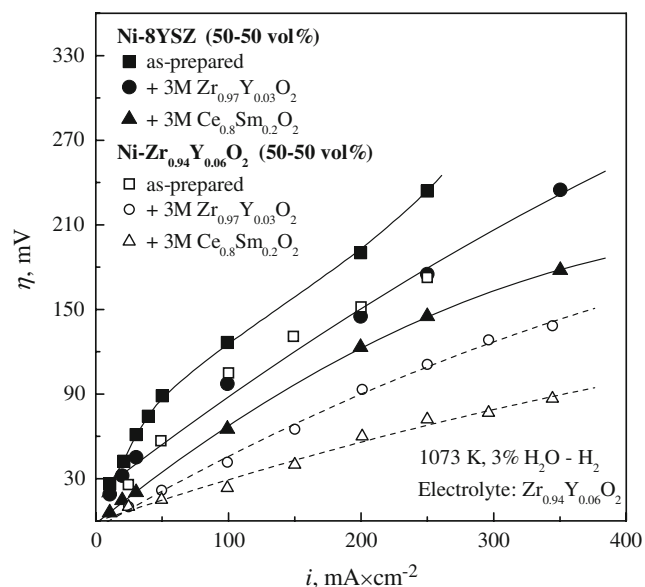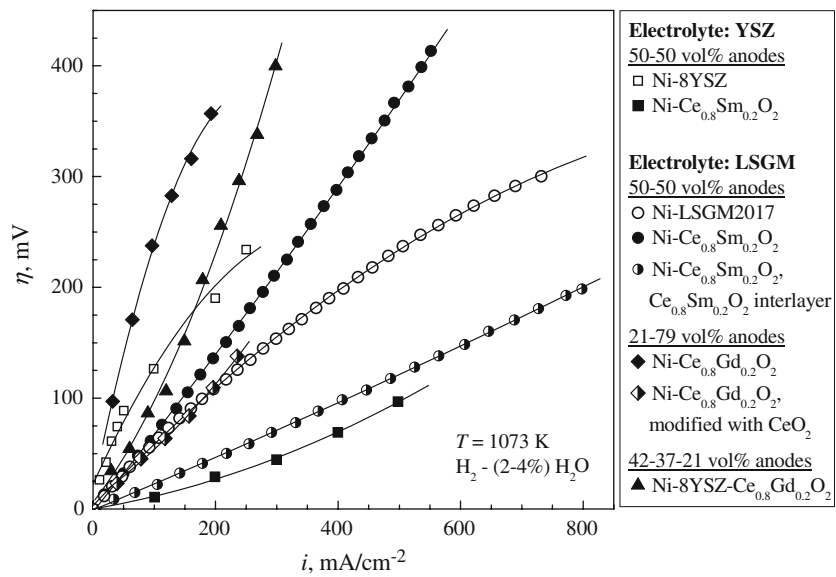

Fig. 7 Current–overpotential dependencies of Ni-YSZ anodes before and after impregnation with 3 M nitrate solutions containing zirconium and yttrium or cerium and samarium cations [214]

at the electrolyte surface; these factors are governed by the electrolyte composition, oxygen partial pressure, overpotential, and temperature. Consequently, the concentration of electronic charge carriers in the electrolyte surface layers may differ substantially from that in the material bulk [230]. The same statement is true for the oxygen vacancies as O_2 molecules may adsorb, dissociate, and incorporate into the solid electrolyte surface either via direct interaction with the vacant sites or via the intermediate complex $O_{ad} - V_O^{\bullet\bullet}$ (see [228] and references cited). The direct oxygen-exchange processes between the electrolyte and gas phase cannot be neglected, at least, for ceria- and lanthanum gallate-based materials (Fig. 10).

The correlations between the solid electrolyte ionic conductivity and electrode kinetics were reported for various galvanic cells with metallic electrodes (e.g., [109, 230] and references cited) and for mixed-conducting $Ln_{0.7}Sr_{0.3}Co_{0.7}Fe_{0.3}O_{3-\delta}$ applied onto $Bi_{1.5}Y_{0.5}O_3$, $BaCe_{0.8}Gd_{0.2}O_3$, $Ce_{0.9}Sr_{0.1}O_2$, and YSZ electrolytes [226]. Although this effect was found insignificant for the zirconia-based materials with rather similar properties [109], an opposite behavior was observed by other authors
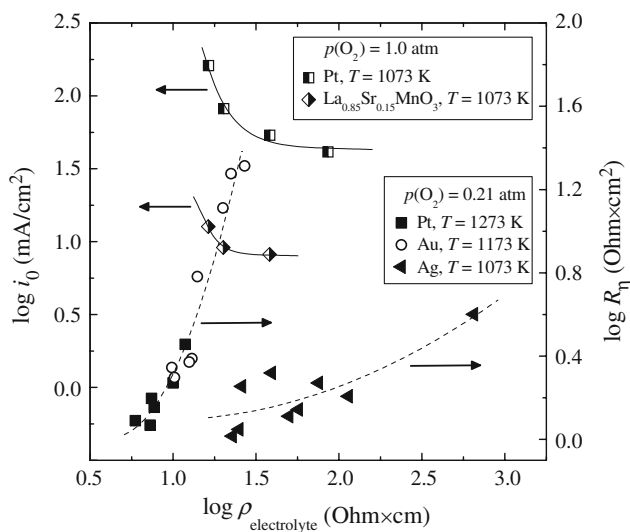

Fig. 9 Polarization resistance [224] and exchange current density [118] of metallic and oxide electrodes vs the solid electrolyte resistivity controlled by Ln^{3+} doping in $Zr(Ln)O_{2-\delta}$
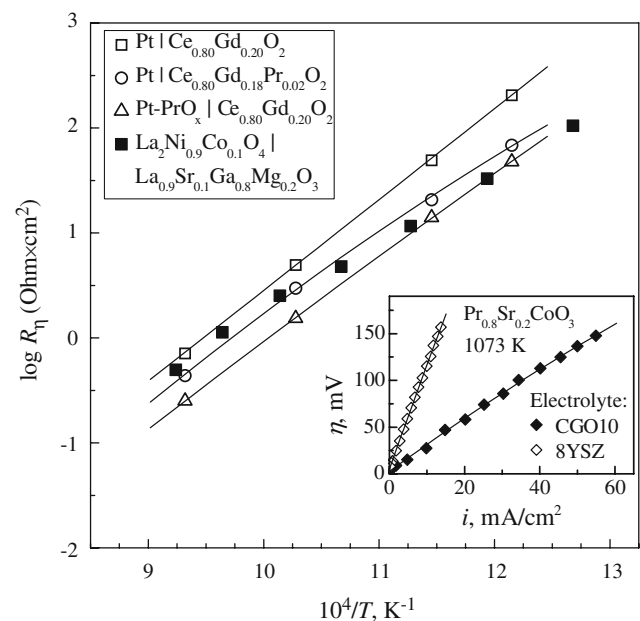

Fig. 10 Temperature dependence of the polarization resistance of porous Pt [231] and $La_2Ni_{0.9}Co_{0.1}O_{4+\delta}$ [232] cathodes in contact with ceria- and lanthanum gallate-based electrolytes in air. The *inset* compares cathodic overpotentials of $Pr_{0.8}Sr_{0.2}CoO_{3-\delta}$ layers applied onto $Ce_{0.9}Gd_{0.1}O_{2-\delta}$ and 8 mol% yttria-stabilized zirconia electrolytes [233]

[38, 118, 224]. The nature was explained in terms of rate-determining charge transfer at the electrode/electrolyte interface [226] and electrocatalytic properties of the electrolyte surface [230]. For example, the exchange currents of Pt or $La_{0.85}Sr_{0.15}MnO_3$ cathodes in contact with yttria- and ytterbia-stabilized zirconia increase proportionally to the electrolyte ionic conductivity, at least below 1173 K [224]; the transport of O^{2-} anions at the electrode/electrolyte interface was suggested to govern cathodic performance when the exchange processes at the electrode surface are fast enough. Analogous tendency was revealed for $Ce_{0.8}Sm_{0.2}O_2$-based anodes applied onto Sc-, Yb-, and Y-doped zirconia, in $H_2O–H_2$ atmospheres [38].

The surface oxygen exchange coefficients of doped ceria are higher than those of zirconia electrolytes [16, 62, 195]. This difference correlates with higher ionic and electronic conductivities of ceria because these properties are all determined, in general, by metal–oxygen bonding energetics. As a result, the fuel cells with CeO_2-based solid electrolytes are characterized with considerably lower polarization with respect to stabilized zirconia. For instance, the R_η values of $La_{0.6}Sr_{0.4}MnO_{3\pm\delta}$ cathode and Ni-YSZ (20–80 wt%) anode at 1073 K were reduced by a factor of 3–21 and 6–150, respectively, when using doped ceria electrolyte or ceria-containing composite [227]. Qualitatively similar results were also obtained for the multilayered cells made of a ceria-based electrolyte with YSZ protective layer at the fuel side [228]. Minor doping of $(La,Sr)(Ga,Mg)O_{3-\delta}$ with iron increases the ionic and electronic conductivities, simultaneously lowering the ohmic losses and anodic overpotentials [82, 225]. The incorporation of variable-valence cations, such as Pr, Mn, Fe, and Co, into YSZ solid electrolyte decreases cathodic polarization of Pt layers up to two to ten times with respect to pure YSZ at 1073 K [234]. This improvement originates, at least partly, from the spreading of the electrode reaction zone due to enhanced electronic conductivity of the electrolyte surface [234]. Again, similar trends are known for ceria-based materials [223, 231].

The correlations between the solid electrolyte composition and electrode performance are often contributed by the materials interaction, resulting in the formation of ion-blocking layers. One classical example is related to the topotactic reaction between perovskite-type $(La,Sr)BO_{3-\delta}$ (B=Mn, Fe, Co) cathodes and ZrO_2-based electrolytes to form lanthanum and strontium zirconates [3, 16, 36, 145, 152, 154]. No blocking layers are expected in the case of doped ceria where, however, cation diffusion from the electrode may decrease ionic conduction [72, 197]. Nonetheless, the relatively low polarization of $Pr_{0.8}Sr_{0.2}CoO_{3-\delta}$ cathodes in contact with $Ce_{0.9}Gd_{0.1}O_{2-\delta}$ compared to YSZ [233] (Fig. 10) becomes possible due to negligible materials interaction. In the case of $(La,Sr)(Ga,Mg)O_{3-\delta}$, the impact of transition metal cations diffusion into the electrolyte depends strongly on their oxidation state and, hence, on the oxygen chemical potential. Under oxidizing conditions, the introduction of cations with moderate oxidation state increases both electronic and ionic conductivities, which may promote oxygen exchange; the higher-valence cations, such as Cr and Mn, decrease ionic transport and exchange currents [127, 212, 235, 236]. In reducing atmospheres, attractive electrochemical properties were observed for Mn-containing LSGM [237], whilst the presence of nickel leads to cell degradation [30, 238]. The oxygen exchange kinetics is also enhanced due to Ba^{2+} incorporation [239]; this explains a high performance of $(La,Ba)CoO_{3-\delta}$ and $YBa(Co,Fe)_4O_{7\pm\delta}$ cathodes in contact with $(La,Sr)(Ga,Mg)O_3$-based electrolytes [199, 203, 240]. The latter effect may also be associated with the formation of peroxide species promoted by the presence of barium [241]. In the case of silicate-based ionic conductors, surface diffusion of Si-containing species onto the electrode surface deteriorates electrochemical activity [84]. Finally, the polarization resistance is often influenced by minor impurities in the solid-electrolyte ceramics. For example, the results of $^{16}O/^{18}O$ exchange studies [242] indicate that the surface exchange rate of YSZ decreases linearly with increasing impurity content, specifically SiO_2, CaO, and Na_2O accumulated at the outermost surface layers. Whatever the microscopic mechanism of phase interaction and segregation, the literature data show that the SOFC components and fabrication conditions should be optimized to suppress these processes. Possible approaches may include chemical etching, minimization of the electrode sintering temperature and time (e.g., via the use of sintering aids), deposition of protective layers between the electrode and electrolyte, and
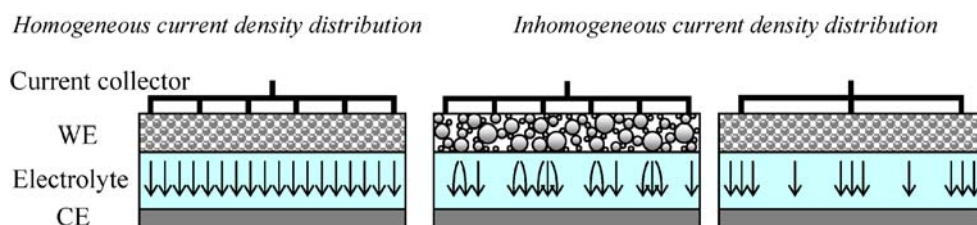

Fig. 11 Schematic illustration of the current constriction effects in the solid-electrolyte membrane for different cathode microstructures and current collector geometry [125]. The *arrows* show the flows of oxygen anions. *WE* and *CE* are the working and counter electrodes, respectively

formation of functionally graded composite microstructures. Particular cases relevant for the practical applications will be considered in the second part of this review.

The importance of current constriction effects for both ohmic and overpotential losses, which may increase on decreasing the contact area between the electrode and current collector, was unambiguously demonstrated using Pt-mesh collectors with different geometric parameters [125]. Assuming that the mean conduction path through the electrode to solid electrolyte is 1/6 of the distance between the nearest-neighboring contacts with current collector, the in-plain resistance of porous layers (R_c) may be estimated as [118]:

$$R_c = \frac{\rho_c}{12 N_c \times d_c} \tag{29}$$

where N_c is the number of square grids per electrode unit area, ρ_c is the specific resistivity, and d_c is the thickness. A small effective electrode area and inhomogeneous current distribution is expected when the number of contacts either with electrolyte or with current collector is insufficient, leading to higher in-plain electrode resistance and a larger ohmic loss in the electrolyte [125]. These problems illustrated schematically in Fig. 11, may be avoided by increasing the electrode layer electronic conductivity. On the other hand, for most electrode materials, the distance between current collector and electrode contacts cannot exceed a critical maximum, usually a few millimeters [41]. Although relatively thick electrodes might, to some extent, act as the current collectors themselves [243], increasing the electrode thickness above a critical limit results in higher polarization, while the ohmic losses (primarily due to electrolyte resistivity) tend to a plateau [125]. Therefore, an optimized microstructure comprising one ultra-thin mixed conductor layer covered by a porous current-collecting layer of coarse grains was suggested for the IT SOFC cathodes [243]. For $Pr_{0.80}Sr_{0.2}MnO_{3\pm\delta}$ cathodes with Pt or Ag meshes or Ag foils as current collectors, increasing the contact area from 4.6% to 27.2% was found to decrease the cell resistance by 7.5 times and to increase power density by four times [244]. In agreement with Sasaki et al. [125], the constriction effect was attributed to discrete contacts between the electrode and current collector; the contact area was found to influence both ohmic resistance and overpotential [244]. The polarization resistance of dense In_2O_3 electrodes was decreased by deposition of Pt onto their surface [245], probably due to similar reasons. Another necessary comment is that volatilization of the current collector components may lead to electrode degradation, particularly to partial blocking of the surface and TPB. This has a key importance for the SOFC stacks with the oxidation-resistant alloys containing chromium, which forms volatile oxide and oxy-hydroxide compounds [246–248].

References

1. Fuel Cell Handbook (2002) EG&G technical services, 6th edn. Science Applications International Corporation, Morgantown, West Virginia
2. Minh NQ, Takahashi T (1995) Science and technology of ceramic fuel cells. Elsevier, Amsterdam
3. Yamamoto O (2000) Electrochim Acta 45:2423
4. Singhal SC (2000) Mater Res Soc Bull 25:16
5. Park S, Vohs JM, Gorte RJ (2000) Nature 404:265
6. Steele BCH (2001) J Mater Sci 36:1053
7. Singhal SC (2002) Solid State Ionics 152–153:405
8. Eguchi K, Kojo H, Takeguchi T, Kikuchi R, Sasaki K (2002) Solid State Ionics 152–153:411
9. Alcaide F, Cabot P-L, Brillas E (2006) J Power Sources 153:47
10. Belmonte M (2006) Adv Eng Mater 8:693
11. von Helmolt R, Eberle U (2007) J Power Sources 165:833
12. Yano M, Tomita A, Sano M, Hibino T (2007) Solid State Ionics 177:3351
13. Baur H, Preis H (1937) Z Elektrochem 6:41
14. Weissbart J, Ruka R (1962) J Electrochem Soc 109:723
15. Möbius H-H (1997) J Solid State Electrochem 1:2
16. Kharton VV, Naumovich EN, Vecher AA (1999) J Solid State Electrochem 3:61
17. Tedmon CS, Spacil HS, Mitoff SP (1969) J Electrochem. Soc. 116:1170
18. Kharton VV, Yaremchenko AA, Naumovich EN (1999) J Solid State Electrochem 3:303
19. Kinoshita K (1992) Electrochemical oxygen technology. Wiley-Interscience, New York
20. Ihringer R, Van herle J, McEvoy AJ (1997) Development of thin film electrolytes co-fired with NiO-YSZ substrates. In: Stimming U, Singhal SC, Tagawa H, Lehnert W (eds) SOFC V. The Electrochemical Society, Pennington, NJ, pp 340–347
21. Kim J-W, Virkar AV, Fung K-Z, Mehta K, Singhal SC (1999) J Electrochem Soc 146:69
22. Doshi R, Richard VL, Carter JD, Wang X, Krumpelt M (1999) J Electrochem Soc 146:1273
23. Van herle J, Ihringer R, Sammes NM, Tompsett G, Kendall K, Yamada K, Wen C, Kawada T, Ihara M, Mizusaki J (2000) Solid State Ionics 132:333
24. Tsai T, Barnett SA (1997) Solid State Ionics 98:191
25. Ishihara T, Honda M, Nishiguchi H, Takita Y (1997) Solid oxide fuel cell operable at decreased temperature using $LaGaO_3$ perovskite oxide electrolyte. In: Stimming U, Singhal SC, Tagawa H, Lehnert W (eds) SOFC V. The Electrochemical Society, Pennington, NJ, pp 301–310
26. Yasuda I, Matsuzaki Y, Yamakawa T, Koyama T (2000) Solid State Ionics 135:381
27. Yu HC, Zhao F, Virkar AV, Fung K-Z (2005) J Power Sources 152:22
28. Madsen BD, Barnett SA (2005) Solid State Ionics 176:2545
29. An S, Lu C, Worrell WL, Gorte RJ, Vohs JM (2004) Solid State Ionics 175:135
30. Huang K, Goodenough JB (2000) J Alloys Compd 303–304:454
31. Bi Z, Cheng M, Dong Y, Wu H, She Y, Yi B (2005) Solid State Ionics 176:655
32. Fukui T, Ohara S, Murata K, Yoshida H, Miura K, Inagaki T (2002) J Power Sources 106:142
33. Steele BCH (2000) Solid State Ionics 129:95
34. McEvoy AJ, Rambert S, Widmer S (1996) Nanostructure, defect chemistry and operating protocols influence SOFC performance. In: Thorstensen B (ed) Proceedings of the 2nd European Solid Oxide Fuel Cell Forum (Oslo, May 1996), vol 1. European SOFC Forum, Oberrohrdorf, Switzerland, pp 599–606

35. Jiang SP (2002) Solid State Ionics 146:1
36. Huijsmans JPP (2001) Curr Opin Solid State Mat Sci 5:317
37. Ishihara T, Shibayama T, Nishiguchi H, Takita Y (2000) Solid State Ionics 132:209
38. Watanabe M, Uchida H, Yoshida M (1997) J Electrochem Soc 144:1739
39. Etsell TH, Flengas SN (1970) Chem Rev 70:339
40. Bouwmeester HJN, Burggraaf AJ (1996) Dense ceramic membranes for oxygen separation. In: Burggraaf AJ, Cot L (eds) Fundamentals of inorganic membrane science and technology. Elsevier, Amsterdam, pp 435–528
41. Perfilyev MV, Demin AK, Kuzin BL, Lipilin AS (1988) High-temperature electrolysis of gases. Nauka, Moscow
42. Adler SB (2004) Chem Rev 104:4791
43. Jiang SP (2007) J Solid State Electrochem 11:93
44. Fergus JW (2006) Solid State Ionics 177:1529
45. Jiang SP (2006) Mater Sci Eng A 418:199
46. Goodenough JB (2003) Annu Rev Mater Res 33:91
47. Kharton VV, Marques FMB, Atkinson A (2004) Solid State Ionics 174:135
48. Fergus JW (2006) J Power Sources 162:30
49. Dalslet B, Blennow P, Hendriksen PV, Bonanos N, Lybye D, Mogensen M (2006) J Solid State Electrochem 10:547
50. Petrov AN, Cherepanov VA, Zuev AYu (2006) J Solid State Electrochem 10:517
51. Liu Y, Tan X, Li K (2006) Catal Rev 48:145
52. Amow G, Skinner SJ (2006) J Solid State Electrochem 10:538
53. Ishihara T, Matsuda H, Takita Y (1994) J Am Chem Soc 116:3801
54. Feng M, Goodenough JB (1994) Eur J Solid State Inorg Chem 31:663
55. Abraham F, Boivin JC, Mairesse G, Nowogrocki G (1990) Solid State Ionics 40–41:934
56. Lacorre P, Goutenoire F, Bohnke O, Retoux R, Laligant Y (2000) Nature 404:856
57. Kramer SA, Tuller HL (1995) Solid State Ionics 82:15
58. Nakayama S, Kageyama T, Aono H, Sadaoka Y (1995) J Mater Chem 5:1801
59. Abram EJ, Sinclair DC, West AR (2001) J Mater Chem 11:1978
60. Tolchard JR, Islam MS, Slater PR (2003) J Mater Chem 13:1956
61. Shaula AL, Kharton VV, Marques FMB (2005) J Solid State Chem 178:2050
62. Kharton VV, Yaremchenko AA, Naumovich EN, Marques FMB (2000) J Solid State Electrochem 4:243
63. Kharton VV, Naumovich EN, Yaremchenko AA, Marques FMB (2001) J Solid State Electrochem 5:160
64. Marozau IP, Marrero-López D, Shaula AL, Kharton VV, Tsipis EV, Núñez P, Frade JR (2004) Electrochim Acta 49:3517
65. Goodenough JB (1997) Solid State Ionics 94:17
66. Badwal SPS (1992) Solid State Ionics 52:23
67. Yamamoto O, Arati Y, Takeda Y, Imanishi N, Mizutani Y, Kawai M, Nakamura Y (1995) Solid State Ionics 79:137
68. Badwal SPS, Ciacchi FT, Milosevic D (2000) Solid State Ionics 136–137:91
69. Mori M, Abe T, Itoh H, Yamomoto O, Takeda Y, Kawahara T (1994) Solid State Ionics 74:157
70. Lee J-H, Yoshimura M (1999) Solid State Ionics 124:185
71. Yahiro H, Eguchi K, Arai H (1989) Solid State Ionics 36:71
72. Kharton VV, Figueiredo FM, Navarro L, Naumovich EN, Kovalevsky AV, Yaremchenko AA, Viskup AP, Carneiro A, Marques FMB, Frade JR (2001) J Mater Sci 36:1105
73. Stevenson JW, Armstrong TR, Pederson LR, Li J, Levinsohn CA, Baskaran S (1998) Solid State Ionics 113–115:571
74. Stevenson JW, Hasinska K, Canfield NL, Armstrong TR (2000) J Electrochem Soc 147:3213
75. Nomura K, Tanase S (1997) Solid State Ionics 98:229
76. Arikawa H, Nishiguchi H, Ishihara T, Takita Y (2000) Solid State Ionics 136–137:31
77. Inaba H, Tagawa H (1996) Solid State Ionics 83:1
78. Hayashi H, Inaba H, Matsuyama M, Lan NG, Dokiya M, Tagawa H (1999) Solid State Ionics 122:1
79. Stevenson JW, Armstrong TR, McGready DE, Pederson LR, Weber WJ (1997) J Electrochem Soc 144:3613
80. Ishihara T, Shibayama T, Honda M, Nishiguchi H, Takita Y (2000) J Electrochem Soc 147:1332
81. Trofimenko N, Ullmann H (1999) Solid State Ionics 118:215
82. Kharton VV, Viskup AP, Yaremchenko AA, Baker RT, Gharbage B, Mather GC, Figueiredo FM, Naumovich EN, Marques FMB (2000) Solid State Ionics 132:119
83. Nguen TL, Dokiya M (2000) Solid State Ionics 132:217
84. Tsipis EV, Kharton VV, Frade JR (2007) Electrochim Acta 52:4428
85. Luebke S, Wiemhoefer H-D (1999) Solid State Ionics 117:229
86. Kim J-H, Yoo H-I (2001) Solid State Ionics 140:105
87. Kharton VV, Tsipis EV, Yaremchenko AA, Vyshatko NP, Shaula AL, Naumovich EN, Frade JR (2003) J Solid State Electrochem 7:468
88. Kharton VV, Shaula AL, Vyshatko NP, Marques FMB (2003) Electrochim Acta 48:1817
89. Shaula AL, Kharton VV, Marques FMB (2006) Solid State Ionics 177:1725
90. Tietz F (1999) Ionics 5:129
91. Hayashi H, Kanoh M, Quan C, Inaba H, Wang S, Dokiya M, Tagawa H (2000) Solid State Ionics 132:227
92. Mori M, Tompsett GM, Sammes NM, Suda E, Takeda Y (2003) Solid State Ionics 158:79
93. Sakaki Y, Takeda Y, Kato A, Imanishi N, Yamamoto O, Hattori M, Ito M, Esaki Y (1999) Solid State Ionics 118:187
94. Tikhonova LA, Samal GI, Zhuk PP, Tonoyan AA, Vecher AA (1990) Inorg Mater 26:149
95. Al Daroukh M, Vashook VV, Ullmann H, Tietz F, Arual Raj I (2003) Solid State Ionics 158:141
96. Aruna ST, Muthuraman M, Patil KC (1999) Solid State Ionics 120:275
97. Tai L-W, Nasrallah MM, Anderson HU, Sparlin DM, Sehlin SR (1995) Solid State Ionics 76:259
98. Tai L-W, Nasrallah MM, Anderson HU, Sparlin DM, Sehlin SR (1995) Solid State Ionics 76:273
99. Petric A, Huang P, Tietz F (2000) Solid State Ionics 135:719
100. Riza F, Ftikos Ch, Tietz F, Fischer W (2001) J Eur Ceram Soc 21:1769
101. Kostogloudis GC, Ftikos Ch, Ahmad-Khanlou A, Naoumidis A, Stöver D (2000) Solid State Ionics 134:127
102. Boehm E, Bassat J-M, Steil MC, Dordor P, Mauvy F, Grenier J-C (2003) Solid State Sci 5:973
103. Skinner SJ, Kilner JA (2000) Solid State Ionics 135:709
104. Yamamoto O, Takeda Y, Kanno R, Kojima T (1989) Stability of perovskite oxide electrode with stabilized zirconia. In: Singhal SC (ed) SOFC I. The Electrochemical Society, Pennington, NJ, pp 242–253
105. Kharton VV, Tsipis EV, Yaremchenko AA, Frade JR (2004) Solid State Ionics 166:327
106. Drennan J, Auchterlonie G (2000) Solid State Ionics 134:75
107. Yuzaki A, Kishimoto A (1999) Solid State Ionics 116:47
108. Murygin IV (1991) Electrode processes in solid electrolytes. Nauka, Moscow
109. Fabry P, Kleitz M (1974) J Electroanal Chem 57:165
110. Perfilyev MV (1978) Tr Inst Elektrokhim Ural Akad Nauk SSSR 26:81
111. Wang DY, Nowick AS (1981) J Electrochem Soc 128:55
112. Mitterdorfer A, Gauckler LJ (1999) Solid State Ionics 117:187

113. Mitterdorfer A, Gauckler LJ (1999) Solid State Ionics 117:203
114. Mizusaki J, Tagawa H, Isobe K, Tajika M, Koshiro I, Maruyama H, Hirano K (1994) J Electrochem Soc 141:1674
115. Horita T, Yamaji K, Sakai N, Xiong Y, Yokokawa H, Kawada T (2002) Ionics 8:108
116. Jiménez R, Kloidt T, Kleitz M (1997) J Electrochem Soc 144:582
117. Yoon SP, Nam SW, Kim S-G, Hong S-A, Hyun S-H (2003) J Power Sources 115:27
118. Kenjo T, Kanehira Y (2002) Solid State Ionics 148:1
119. Steele BCH (1997) Solid State Ionics 94:239
120. Simner SP, Anderson MD, Pederson LR, Stevenson JW (2005) J Electrochem Soc 152:A1851
121. Adler SB, Lane JA, Steele BCH (1996) J Electrochem Soc 143:3554
122. Liu M (1998) J Electrochem Soc 145:142
123. Chan SH, Khor KA, Xia ZT (2001) J Power Sources 93:130
124. Ni M, Leung MKH, Leung DYC (2007) J Power Sources 168:369
125. Sasaki K, Wurth J-P, Gschwend R, Gödickemeier M, Gauckler LJ (1996) J Electrochem Soc 143:530
126. Svensson AM, Nişancioğlu K (1998) J Electrochem Soc 145:3130
127. Kharton VV, Tsipis EV, Marozau IP, Viskup AP, Frade JR, Irvine JTS (2007) Solid State Ionics 178:101
128. Mizusaki J, Saito T, Tagawa H (1996) J Electrochem Soc 143:3065
129. Luerssen B, Janek J, Imbihl R (2001) Solid State Ionics 141:701
130. Janek J, Rohnke M, Luerssen B, Imbihl R (2000) Phys Chem Chem Phys 2:1935
131. Chebotin VN, Perfiliev MV (1978) Electrochemistry of solid electrolytes. Technical Information Center, US Department of Energy, Oak Ridge
132. Marczewski AW, Derylo-Marczewska A, Jaroniec M (1988) Chem Scripta 28:173
133. Endo A, Fukunaga H, Wen C, Yamada K (2000) Solid State Ionics 135:353
134. Atangulov RU, Murygin IV (1993) Solid State Ionics 67:9
135. Chang C-L, Lee T-C, Huang T-J (1998) J Solid State Electrochem 2:291
136. Gödickemeier M, Sakai K, Gauckler LJ, Riess I (1997) J Electrochem Soc 144:1635
137. Svensson AM, Sunde S, Nişancioğlu K (1997) J Electrochem Soc 144:2719
138. Svensson AM, Sunde S, Nişancioğlu K (1998) J Electrochem Soc 145:1390
139. Mizusaki J, Amato K, Yamauchi S, Fueki K (1987) Solid State Ionics 22:313
140. Fleig J (2002) J Power Sources 105:228
141. Fleig J, Maier J (2004) J Eur Ceram Soc 24:1343
142. Siebert E, Hammouche A, Kleitz M (1995) Electrochim Acta 40:1741
143. Coffey GW, Pederson LR, Rieke PC (2003) J Electrochem Soc 150:A1139
144. Kuznecov M, Otschik P, Obenaus P, Eichler K, Schaffrath W (2003) Solid State Ionics 157:371
145. van Heuveln FH, Bouwmeester HJM (1997) J Electrochem Soc 144:134
146. Jiang SP, Love JG, Ramprakash Y (2002) J Power Sources 110:201
147. Chen XJ, Khor KA, Chan SH (2003) J Power Sources 123:17
148. Kamata H, Hosaka A, Mizusaki J, Tagawa H (1998) Solid State Ionics 106:237
149. Murray E, Tsai T, Barnett S (2002) Solid State Ionics 110:235
150. Takeda Y, Kanno R, Noda M, Tomida Y, Yamamoto O (1987) J Electrochem Soc 134:2656
151. Tsuneyoshi K, Mori K, Sawata A, Mizusaki J, Tagawa H (1989) Solid State Ionics 35:263
152. Mizusaki J, Tagawa H, Katou M, Hirano K, Sawata A, Tsuneyoshi K (1991) Electrochemical properties of some perovskite-type oxides as oxygen gas electrodes on yttria stabilized zirconia. In: Grosz F, Zegers P, Singhal SC, Yamamoto O (eds) SOFC II. The Electrochemical Society, Pennington, NJ, pp 487–494
153. Fukunaga H, Koyama M, Takahashi N, Wen C, Yamada K (2000) Solid State Ionics 132:279
154. Adler SB (1998) Solid State Ionics 111:125
155. Adler SB (2000) Solid State Ionics 135:603
156. Jamnik J, Maier J (2001) Phys Chem Chem Phys 3:1668
157. Baker R, Guindet J, Kleitz M (1997) J Electrochem Soc 144:2427
158. Mogensen M, Skaarup S (1996) Solid State Ionics 86–88:1151
159. Brown M, Primdahl S, Mogensen M (2000) J Electrochem Soc 147:475
160. de Boer B, Gonzalez M, Bouwmeester HJM, Verweij H (2000) Solid State Ionics 127:269
161. Mohamedi-Boulenouar FZ, Guindet J, Hammou A (1997) Influence of water vapor on electrochemical oxidation of hydrogen at the Ni/zirconia interface. In: Stimming U, Singhal SC, Tagawa H, Lehnert W (eds) SOFC V. The Electrochemical Society, Pennington, NJ, pp 441–450
162. Mizusaki J, Tagawa H, Saito T, Kamitani K, Yamamura T, Hirano K, Ehara S, Takagi T, Hikita T, Ippommatsu M, Nakagawa S, Hashimoto K (1994) J Electrochem Soc 141:2129
163. Bieberle A, Meier LP, Gauckler LJ (2001) J Electrochem Soc 148:A646
164. Primdahl S, Mogensen M (1997) J Electrochem Soc 144:3409
165. Ihara M, Kusano T, Yokoyama C (2001) J Electrochem Soc 148:A209
166. Jiang SP, Ramprakash Y (1999) Solid State Ionics 122:211
167. Jiang SP, Ramprakash Y (1999) Solid State Ionics 116:145
168. Iwata T (1996) J Electrochem Soc 143:1521
169. Jung GB, Lo KF, Chan SH (2007) J Solid State Electrochem 11:1435
170. Williford RE, Chick LA, Maupin GD, Simner SP, Stevenson JW (2003) J Electrochem Soc 150:A1067
171. Mogensen M, Kammer K (2003) Annu Rev Mater Res 33:321
172. Yentekakis IV, Jiang Y, Neophytides S, Bebelis S, Vayenas CG (1995) Ionics 1:491
173. Murray EP, Tsai T, Barnett SA (1999) Nature 400:649
174. Liu J, Barnett SA (2003) Solid State Ionics 158:11
175. Vernoux P, Guindet J, Gehain E, Kleitz M (1997) Catalysts for continuous methane reforming in medium temperature SOFC. In: Stimming U, Singhal SC, Tagawa H, Lehnert W (eds) SOFC V. The Electrochemical Society, Pennington, NJ, pp 219–227
176. Sato K, Nakamura J, Uchijima T, Hayakawa T, Hamakawa S, Tsunoda T, Shishido T, Takehira K (2000) Solid State Ionics 136–137:753
177. Diskin AM, Cunningham RH, Ormerod RM (1998) Catal Today 46:147
178. Finnerty CM, Coe NJ, Cunningham RH, Ormerod RM (1998) Catal Today 46:137
179. Chan SH, Xia ZT (2001) J Electrochem Soc 148:A388
180. Arnošt D, Schneider P (1995) Chem Eng J 57:91
181. Drescher I, Lehnert W, Meusinger J (1998) Electrochim Acta 43:3059
182. Eguchi K, Kunisa Y, Adachi K, Arai H (1996) J Electrochem Soc 143:3699
183. Wen C, Kato R, Fukunaga H, Ishitani H, Yamada K (2000) J Electrochem Soc 147:2076
184. Bieberle A, Gaukler LJ (2002) Solid State Ionics 146:23
185. Jiang SP, Badwal SPS (1999) Solid State Ionics 123:209
186. Holtappels P, de Haart LGJ, Stimming U (1999) J Electrochem Soc 146:1620

187. Charpentier P, Fragnaud P, Schleich DM, Gehain E (2000) Solid State Ionics 135:373
188. Mizusaki J, Tagawa H, Miyaki Y, Yamauchi S, Fueki K, Koshiro I, Hirano K (1992) Solid State Ionics 53–56:126
189. Deutschmann O, Behrendt F, Warnatz J (1998) Catal Today 46:155
190. Peña MA, Gómez JP, Fierro JLG (1996) Appl Catal A 144:7
191. York APE, Xiao T, Green MLH (2003) Top Catal 22:345
192. Kharton VV, Naumovich EN, Samokhval VV (1997) Solid State Ionics 99:269
193. Lee HY, Cho WS, Oh SM, Wiemhöfer H-D, Göpel W (1995) J Electrochem Soc 142:2659
194. Bouwmeester HJM, Kruidhof H, Burggraaf AJ (1994) Solid State Ionics 72:185
195. Steele BCH (1995) Solid State Ionics 75:157
196. Kharton VV, Shaula AL, Naumovich EN, Vyshatko NP, Marozau IP, Viskup AP, Marques FMB (2003) J Electrochem Soc 150:J33
197. Shaula AL, Kharton VV, Marques FMB, Kovalevsky AV, Viskup AP, Naumovich EN (2006) J Solid State Electrochem 10:28
198. Marozau IP, Kharton VV, Viskup AP, Frade JR, Samakhval VV (2006) J Eur Ceram Soc 26:1371
199. Tsipis EV, Kharton VV, Frade JR, Núñez P (2005) J Solid State Electrochem 9:547
200. Tikhonovich VN, Kharton VV, Naumovich EN, Savitsky AA (1998) Solid State Ionics 106:197
201. Yasuda I, Ogasawara K, Hishinuma M, Kawada T, Dokiya M (1996) Solid State Ionics 86–88:1197
202. Ullmann H, Trofimenko N, Tietz F, Stöver D, Ahmad-Khanlou A (2000) Solid State Ionics 138:79
203. Ishihara T, Fukui S, Nishiguchi H, Takita Y (2002) Solid State Ionics 152–153:609
204. Kharton VV, Naumovich EN, Vecher AA, Nikolaev AV (1995) J Solid State Chem 120:128
205. Teraoka Y (1991) Solid State Ionics 48:207
206. Lee HY, Oh SM, Seo I, Rocholl F, Wiemhöfer H-D (1997) The cathodic activity and interfacial stability of Y0.8Ca0.2Co1-xFexO3/YSZ electrodes. In: Stimming U, Singhal SC, Tagawa H, Lehnert W (eds) SOFC V. The Electrochemical Society, Pennington, NJ, pp 520–529
207. Ioroi T, Hara T, Uchimoto Y, Ogumi Z, Takehara ZI (1998) J Electrochem Soc 145:1999
208. Endo A, Wada S, Wen C, Komiyama H, Yamada K (1998) J Electrochem Soc 145:L35
209. Adler SB, Chen XY, Wilson JR (2007) J Catal 245:91
210. De Souza RA (2006) Phys Chem Chem Phys 8:890
211. Kharton VV, Marques FMB (2002) Curr Opin Solid State Mater Sci 6:261
212. Bronin DI, Kuzin BL, Yaroslavtsev IYu, Bogdanovich NM (2006) J Solid State Electrochem 10:651
213. Simwonis D, Tietz F, Stöver D (2000) Solid State Ionics 132:241
214. Jiang SP, Duan YY, Love JG (2002) J Electrochem Soc 149:A1175
215. Kharton VV, Naumovich EN, Tikhonovich VN, Bashmakov IA, Boginsky LS, Kovalevsky AV (1999) J Power Sources 79:242
216. Marina OA, Bagger C, Primdahl S, Mogensen M (1999) Solid State Ionics 123:199
217. Gorte RJ, Park S, Vohs JM, Wang C (2000) Adv Mater 12:1465
218. Wang S, Kato T, Nagata S, Honda T, Kaneko T, Iwashita N, Dokiya M (2002) J Electrochem Soc 149:A927
219. Tsipis EV, Kharton VV, Frade JR (2005) J Eur Ceram Soc 25:2623
220. Maric R, Ohara S, Fukui T, Inagaki T, Fujita J (1998) Electrochem Solid-State Lett 1:201
221. Tsipis EV, Kharton VV, Bashmakov IA, Naumovich EN, Frade JR (2004) J Solid State Electrochem 8:674
222. Primdahl S, Mogensen M (2002) Solid State Ionics 152:597
223. Fagg DP, Kharton VV, Frade JR (2004) J Solid State Electrochem 8:618
224. Uchida H, Yoshida M, Watanabe M (1999) J Electrochem Soc 146:1
225. Ishihara T, Shibayama T, Honda M, Nishiguchi H, Takita Y (2000) J Electrochem Soc 147:1332
226. Liu M, Wu Z (1998) Solid State Ionics 107:105
227. Mishima Y, Mitsuyasu H, Ohtaki M, Eguchi K (1998) J Electrochem Soc 145:1004
228. Tsai T, Perry E, Barnett S (1997) J Electrochem Soc 144:L130
229. Horita T, Yamaji K, Sakai N, Yokokawa H, Kawada T, Kato T (2000) Solid State Ionics 127:55
230. Schouler EJL (1983) Solid State Ionics 9–10:945
231. Kharton VV, Viskup AP, Figueiredo FM, Naumovich EN, Shaulo AL, Marques FMB (2002) Mater Lett 53:160
232. Amow G, Whitfield PS, Davidson IJ, Hammond RP, Munnings CN, Skinner SJ (2004) Ceram Int 30:1635
233. Qiu L, Ichikawa T, Hirano S, Imanishi N, Takeda Y (2003) Solid State Ionics 158:55
234. Bohac P, Orliukas A, Gauckler L (1994) Lowering of the cathode overpotential of SOFC by electrolyte doping. In: Waser R, Hoffmann S, Bonnenberg D, Hoffmann Ch (eds) Electroceramics IV, vol II. IWE, University of Technology, Augustinus Buchhandlung, Aachen, pp 771–780
235. Kharton VV, Yaremchenko AA, Viskup AP, Mather GC, Naumovich EN, Marques FMB (2001) J Electroceramics 7:57
236. Naumovich EN, Kharton VV, Yaremchenko AA, Patrakeev MV, Kellerman DG, Logvinovich DI, Kozhevnikov VL (2006) Phys Rev B 74:064105
237. Chen F, Liu M (1998) J Solid State Electrochem 3:7
238. Huang P, Horky A, Petric A (1999) J Am Ceram Soc 82:2402
239. Yamaji K, Horita T, Sakai N, Yokokawa H (2002) Solid State Ionics 152–153:517
240. Tsipis EV, Kharton VV, Frade JR (2006) Solid State Ionics 177:1823
241. Grasset F, Dussarrat C, Darriet J (1997) J Mater Chem 7:1911
242. de Ridder M, Vervoort AGJ, van Welzenis RG, Brongersma HH (2003) Solid State Ionics 156:255
243. Kleitz M, Petitbon F (1996) Solid State Ionics 92:65
244. Jiang SP, Love JG, Apateanu L (2003) Solid State Ionics 160:15
245. Bronin DI, Kuzin BL, Näfe H, Aldinger F (1998) Ionics 4:249
246. Matsuzaki Y, Yasuda I (2001) J Electrochem Soc 148:A126
247. Jiang SP, Zhang JP, Föger K (2000) J Electrochem Soc 147:3195
248. Larring Y, Haugsrud R, Norby T (2003) J Electrochem Soc 150:B374